NASA Grant NAG3-1671

Unsteady Blade Row Interaction in a Transonic Turbine

Final Report

15 July 1996

Daniel J. Dorney
Department of Mechanical & Aeronautical Engineering
Western Michigan University
Kalamazoo, MI 49008-5065

Prepared for
NASA Lewis Research Center
Cleveland, OH 44135

Contents

List of Tables

List of Figures

NOMENCLATURE

a	- Speed of sound
e_t	- Total energy
M	- Mach number
N	- Number of film cooling holes
P	- Static pressure
Re	- Inlet reference Reynolds number
S	- Local blade span
T	- Static temperature
u, v, w	- x, y, z components of velocity
W	- Mass flow
β	- Pitch angle
η	- Turbine efficiency
ψ	- Yaw angle
ρ	- Density
τ	- Shear stress
Ω	- Rotor rotational speed

SUBSCRIPTS

in	- Inlet
out	- Exit
t	- time derivative
T	- Stagnation quantity
TT	- Referenced to inlet/exit total quantities
x, y, z	- First derivative with respect to x, y, z
∞	- Inlet free stream quantity

ABSTRACT

Experimental data from jet-engine tests have indicated that unsteady blade row interaction effects can have a significant impact on the performance of multiple-stage turbines. The magnitude of blade row interaction is a function of both blade-count ratio and axial spacing. In the current research program, numerical simulations have been used to quantify the effects of blade count ratio on the performance of an advanced turbine geometries.

INTRODUCTION

The need for improved durability and reduced noise levels has motivated engineers to assess the effects of flow unsteadiness on the performance of turbomachinery components. The aerodynamic interaction between adjacent blade rows can lead to a reduction of efficiency and noise generation in turbine stages. The two principal types of aerodynamic interaction are usually referred to as potential-flow and wake interaction. Potential-flow interaction results from the variations in the velocity potential or pressure fields associated with the blades of a neighboring row, and their effect upon the blades of a given row moving at a different rotational speed. This type of interaction is of serious concern when the axial spacing between adjacent blade rows is small or the axial flow Mach number is high. Wake interaction is the effect upon the flow through a downstream blade row of the vortical and entropic wakes shed by one or more upstream rows.

The focus of the two-year effort has been to use two- and three-dimensional viscous, unsteady vane/blade interaction numerical analyses to identify and alleviate the sources of harmful aerodynamic interactions in an advanced turbine design. The goal of this final progress report is to summarize the results of only the three-dimensional flow simulations.

NUMERICAL INTEGRATION PROCEDURE

Governing Equations

The governing equations considered in this study are the time dependent, three-dimensional Reynolds-averaged Navier-Stokes equations:

$$U_t + (F_i + F_v)_x + (G_i + G_v)_y + (H_i + H_v)_z = 0 \tag{1}$$

where

$$U = \begin{bmatrix} \rho \\ \rho u \\ \rho v \\ \rho w \\ e_t \end{bmatrix} \tag{2}$$

$$F_i = \begin{bmatrix} \rho u \\ \rho u^2 + P \\ \rho uv \\ \rho uw \\ (e_t + P)u \end{bmatrix} \quad F_v = - \begin{bmatrix} 0 \\ \tau_{xx} \\ \tau_{xy} \\ \tau_{xz} \\ \tau_{hx} \end{bmatrix} \tag{3}$$

$$G_i = \begin{bmatrix} \rho v \\ \rho uv \\ \rho v^2 + P \\ \rho vw \\ (e_t + P)v \end{bmatrix} \quad G_v = - \begin{bmatrix} 0 \\ \tau_{yx} \\ \tau_{yy} \\ \tau_{yz} \\ \tau_{hy} \end{bmatrix} \tag{4}$$

$$H_i = \begin{bmatrix} \rho w \\ \rho uw \\ \rho vw \\ \rho w^2 + P \\ (e_t + P)w \end{bmatrix} \quad H_v = - \begin{bmatrix} 0 \\ \tau_{zx} \\ \tau_{zy} \\ \tau_{zz} \\ \tau_{hz} \end{bmatrix} \tag{5}$$

where

$$\begin{aligned}
\tau_{xx} &= 2\mu u_x + \lambda (u_x + v_y + w_z) \\
\tau_{xy} &= \mu (u_y + v_x) \\
\tau_{xz} &= \mu (u_z + w_x) \\
\tau_{yx} &= \tau_{xy} \\
\tau_{yy} &= 2\mu v_y + \lambda (u_x + v_y + w_z) \\
\tau_{yz} &= \mu (v_z + w_y) \\
\tau_{zx} &= \tau_{xz} \\
\tau_{zy} &= \tau_{yz} \\
\tau_{zz} &= 2\mu w_z + \lambda (u_x + v_y + w_z) \\
\tau_{hx} &= u\tau_{xx} + v\tau_{xy} + w\tau_{xz} + \gamma\mu {P_r}^{-1} e_x \\
\tau_{hy} &= u\tau_{yx} + v\tau_{yy} + w\tau_{yz} + \gamma\mu {P_r}^{-1} e_y \\
\tau_{hz} &= u\tau_{zx} + v\tau_{zy} + w\tau_{zz} + \gamma\mu {P_r}^{-1} e_z \\
e &= \frac{P}{(\rho(\gamma - 1))} \\
e_t &= \rho e + \frac{\rho(u^2 + v^2 + w^2)}{2}
\end{aligned} \tag{6}$$

For the present application, the second coefficient of viscosity is calculated using Stokes' hypothesis, $\lambda = -2/3\mu$. The equations of motion are completed by the perfect gas law.

The viscous fluxes are simplified by incorporating the thin layer assumption [1]. In the current study, viscous terms are retained only in the direction normal to the hub surfaces and in the direction normal to the blade surfaces. To extend the equations of motion to turbulent flows, an eddy viscosity formulation is used. Thus, the effective viscosity and effective thermal conductivity can be defined as:

$$\begin{aligned} \mu &= \mu_L + \mu_T \\ \frac{\kappa}{c_p} &= \frac{\mu_L}{P_{rL}} + \frac{\mu_T}{P_{rT}} \end{aligned} \tag{7}$$

The turbulent viscosity, μ_T, is calculated using the Baldwin-Lomax two-layer algebraic turbulence model [1].

Solution Procedure

The numerical algorithm used in the three-dimensional computational procedure consists of a time-marching, implicit, finite-difference scheme. The procedure is third-order spatially accurate and first-order temporally accurate. The inviscid fluxes are discretized according to the upwind scheme developed by Roe [2]. The viscous fluxes are calculated using standard central differences. An alternating direction, approximate-factorization technique is used to compute the time rate changes in the primary variables. Newton sub-iterations are used at each global time step to increase stability and reduce linearization errors. For all cases investigated in this study, two Newton sub-iterations were performed at each time step. Further details of the numerical techniques can be found in Rai [3] and Dorney *et al.* [4, 5].

Boundary Conditions

The theory of characteristics is used to determine the boundary conditions at the vane inlet and blade exit. For subsonic inlet flow four quantities are specified and one is extrapolated from the interior of the computational domain. The total pressure (or entropy, s), v and w velocity components (or the corresponding tangential and meridional angles) and the downstream running Riemann invariant, $R_1 = u + \frac{2a}{\gamma-1}$ (or the total temperature T_t), are specified as a function of the radius. The upstream running Riemann invariant, $R_2 = u - \frac{2a}{\gamma-1}$, is extrapolated from the interior of the computational domain.

For subsonic outflow one flow quantity is specified and four are extrapolated from the interior of the computational domain. The v and w velocity components, entropy, and the downstream running Riemann invariant are extrapolated from the interior of the computational domain. The pressure ratio, P_2/P_{t0}, is specified at mid-span of the computational exit and the pressure at all other radial locations at the exit is obtained by integrating the equation for radial equilibrium. Periodicity is enforced along the outer boundaries of the H-grids in the circumferential (θ) direction.

For viscous simulations, no-slip boundary conditions are enforced along the surfaces of the vane and blade airfoils. Absolute no-slip boundary conditions are enforced at the hub and tip endwalls of the vane region, along the surface of the vane, and along the outer casing (tip endwall) of the rotor blade. Relative no-slip boundary conditions are imposed at the

hub and along the surface of the rotor blade. It is assumed that the normal derivative of the pressure is zero at solid wall surfaces. In addition, a specified (zero) heat flux distribution is held constant in time along the solid surfaces. Film cooling is simulated using transpiration conditions at discrete grid points.

The flow variables of Q at zonal boundaries are explicitly updated after each time step by interpolating values from the adjacent grid. The zonal boundary conditions are non-conservative, but have been determined to be accurate for transonic flows [6, 7].

Grid Generation

The Navier-Stokes analysis uses overlaid zonal grids to discretize the vane-blade flow field and facilitate relative motion of the rotor [8]. A combination of O- and H-grid sections are generated at constant radial spanwise locations in the blade-to-blade direction extending upstream of the vane leading edge to downstream of the rotor blade trailing edge. Algebraically generated H-grids are used in the regions upstream of the leading edge, downstream of the trailing edge and in the inter-blade region. The O-grids, which are body-fitted to the surfaces of the airfoils and generated using an elliptic equation solution procedure, are used to properly resolve the viscous flow in the blade passages and to easily apply the algebraic turbulence model. Computational grid lines within the O-grids are stretched in the blade-normal direction with a fine grid spacing at the wall. The combined H- and O- overlaid grid sections are stretched in the spanwise direction away from the hub and tip regions with a fine grid spacing located adjacent to the hub and tip. An O-grid structure is used in the region between the rotor blade and the tip endwall in the tip clearance region.

The computational grid for the first (EMD or RED) configuration, which consists of 2 high-pressure turbine (HPT) vanes, 3 HPT rotors, 2 low-pressure turbine (LPT) vanes and 3 LPT rotors, contains approximately 3.2 million grid points [8]. The computational grid for the redesigned (FFR or BLUE) configuration, which consists of 4 HPT vanes, 5 HPT rotors, 4 LPT vanes and 4 LPT rotors, contains approximately 3.7 million grid points [9].

THREE-DIMENSIONAL SIMULATIONS

Three sets of three-dimensional simulations have been performed for the EMD and FFR geometries, including

- steady multiple-stage simulations without film cooling
- steady multiple-stage simulations with film cooling
- unsteady multiple-stage simulations with film cooling

The three-dimensional simulations were performed on the NAS Cray C90 located at NASA Ames Research Center. The steady simulations were run until the solutions became invariant, while the unsteady simulations were run until the solutions reached a marginally periodic state (approximately 3 blade-passing cycles). Although this is the final report of the grant, the unsteady simulations will be continued in the deferred queue on the NAS Cray C90 until the end of the operational year (October). The extremely numerical large data base generated during the course of these simulations will be transferred to tape and made available to interested parties.

Film Cooling Parameters

The film cooling parameters are based on the design data for both configurations [10]. Tables 1 and 2 contain the specified injection parameters for the EMD and FFR geometries, respectively. In both tables, the angles α_1 and α_2 refer to the flow injection angles in the streamwise and radial directions, respectively. The angles are measured with respect to the local surface tangents. Thus, the film cooling fluid is injected in the streamwise direction at an angle of 10 degrees. The injection angle is large enough to be realistic, yet small enough to not disturb the boundary layer. The pressure at the injection locations is specified to be equal to the value of the pressure without fluid injection, and the density is determined from the perfect gas law. The injection velocity is determined from the calculated density, the area of the control surface and the specified mass flow ($dW/(NW_{inlet})$, where W is the mass flow and N is the number of film cooling holes.

The film cooling holes are located between 20% and 80% of the span. In both geometries each HPT vane contains 112 film cooling holes, each HPT blade contains 120 film cooling holes, each LPT vane contains 120 film cooling holes and each LPT blade contains 64 film cooling holes. Thus, the 2-3-2-3 EMD geometry is modeled with a total of 1016 film cooling holes, while the 4-5-4-4 FFR geometry contains a total of 1784 film cooling holes.

Aerodynamic Data

Tables 3-8 contain the steady and time-averaged flow quantities at the inlet and exit (midspan) of each blade row for the six simulations. Although there are differences between the steady and unsteady results, the predicted data shows reasonable agreement with the results of the two-dimensional simulations [11]. Table 9 contains the predicted efficiencies for each of the simulations. The efficiencies of the FFR design are uniformly higher than those of the EMD configurations. In the unsteady simulations, there appear to be large differences between the HPT and LPT efficiencies. There are several factors which must be considered when interrogating the distribution of the efficiencies predicted in the unsteady simulations, including

- The flow variables used to predict the efficiency are taken at the inlet and exit of each blade row. However, in the endwall regions between rotating and non-rotating components the rotation speed is gradually varied to avoid excessive velocity gradients. This process causes local jumps in the total pressure and total temperature near the endwalls.

- The total pressure and total pressure are currently area-averaged in both the circumferential and radial directions. There may be other methods, such as mass averaging, which are better suited for three-dimensional simulations.

Although the absolute values of the predicted efficiencies may not be correct, the trends do indicate improved flow characteristics of the FFR design.

Figures 1-3 contain the time-averaged surface pressure coefficient distributions for the EMD configuration at 10%, 50% and 90% of the span, respectively. In this study, the pressure coefficient is defined as

$$C_p = \frac{P_{avg} - P_{t\infty}}{\frac{1}{2}\rho_\infty U^2} \tag{8}$$

Figures 4-6 show the surface pressure coefficient distributions for the corresponding spanwise locations of the FFR geometry. While the midspan data show reasonable agreement with the two-dimensional results [11], large spanwise variations are observed in the pressure distributions (especially on the HPT blades and LPT vanes).

Figures 7-30 contain the time-averaged radial distributions of the total pressure, total temperature, Mach number and pitch angle at the exit of each blade row in the EMD configuration. For the HPT and LPT rotor blades, both absolute and relative frame profiles are included. Note, the radial profiles are averaged separately in each blade passage of a given blade row. Differences between the time-averaged profiles in a given blade row usually indicate that: 1) the solution is not completely time periodic, 2) the solution contains frequencies other than the blade passing frequency (*i.e.,* trailing edge shedding, shock reflections, etc.), or 3) a combination of both phenomena. The profiles for the HPT vane indicate a large loss region in the tip region (see Figs. 7-10). At the exit of the HPT blade, the largest losses are observed in the hub region (see Figs. 11-18). The large total temperature variations and decreased Mach numbers near the hub are also an indication of high losses; and to some extent these variables provide information about the path of the secondary flows. In the LPT vane and blade passages the losses appear to be evenly distributed across the span of the airfoils (see Figs. 19-30). However, large spanwise variations in the total temperature and pitch angle are evident at the exit of the LPT blade; especially near the hub, which indicates a large region of secondary flow.

Figures 31-54 contain the time-averaged radial distributions of the total pressure, total temperature, Mach number and pitch angle at the exit of each blade row in the FFR configuration. The losses in the HPT vane are relatively constant across the span (see Figs. 31-34, while the HPT blade exhibits a pocket of higher losses near 25% of the span (see Figs. 35-42). In general, the spanwise distribution of the losses (and other flow variables) at the exit of the HPT in the FFR design are smoother than those obtained in the EMD configuration. The losses in the LPT vane are nearly constant across the span (see Figs. 43-46), while the LPT blade shows an elevated loss region near 25% of the span (see Figs. 47-54). Again, the total temperature, Mach number and pitch angle profiles indicate rather strong secondary flows in the hub region of the LPT blade passage.

Figures 55-62 illustrate instantaneous static pressure and entropy contours for the first blade passage of each blade row in the EMD configuration, while Figs. 63-70 contain the corresponding contours for the FFR design.

CONCLUSIONS

A series of three-dimensional flow simulations, including film cooling, have been performed for two advanced transonic turbine geometries. The predicted results indicated significantly better performance of the FFR design compared to the EMD geometry. These results support the conclusions of a series of two-dimensional simulations, which indicated that the performance increases were the result of weakened pressure and shock reflections off the low-pressure turbine vane.

References

[1] Baldwin, B. S. and Lomax, H., "Thin-Layer Approximation and Algebraic Model for Separated Turbulent Flows," AIAA Paper 78-257, 1978.

[2] Roe, P. L., "Approximate Riemann Solvers, Parameter Vectors, and Difference Schemes," *Journal of Computational Physics*, Vol. 43, 1981, pp. 357-372.

[3] Rai, M. M., "Three-Dimensional Navier-Stokes Simulations of Turbine Rotor-Stator Interaction," *AIAA Journal of Propulsion and Power* Vol. 5, 1989, pp. 307-319.

[4] Dorney, D. J., Davis, R. L., Edwards, D. E. and Madavan, N. K., "Unsteady Analysis of Hot Streak Migration in a Turbine Stage," *AIAA Journal of Propulsion and Power*, Vol. 8, No. 2, 1992, pp. 520-529.

[5] Dorney, D. J., and Davis, R. L., "Numerical Simulation of Turbine 'Hot Spot' Alleviation Using Film Cooling," *AIAA Journal of Propulsion and Power*, Vol. 9, No. 3, 1993, pp. 329-336.

[6] Steinke, R. J., "Application of a Two-Dimensional Unsteady Viscous Analysis Code to a Supersonic Throughflow Fan Stage," NASA TM 4141, 1989.

[7] Dorney, D. J., and Davis, R. L., "Numerical Simulations of Unsteady Transonic Flows in Turbomachines," AIAA Paper 94-2833, 1994.

[8] Dorney, D. J., *Unsteady Blade Row Interaction in a Transonic Turbine,* NAG3-1671 Progress Report 5, March 6, 1995.

[9] Dorney, D. J., *Unsteady Blade Row Interaction in a Transonic Turbine,* NAG3-1671 Progress Report 7, October 16, 1995.

[10] Rowey, R. J., Pratt & Whitney, Private Communication, April, 1995.

[11] Dorney, D. J., *Unsteady Blade Row Interaction in a Transonic Turbine,* NAG3-1671 Progress Report 4, January 31, 1995.

P&W/ATFE Competition Sensitive Data

	HPT vane	HPT blade	LPT vane	LPT blade
T_{inj} (R)	1540.1	1546.1	1997.9	1361.4
dW/W_{inlet} (prs)	0.0995	0.0859	0.03468	0.01157
dW/W_{inlet} (sct)	0.0250	0.0093	0.03468	—
$(\alpha_1)_{inj}$ (deg)	10.0	10.0	10.0	10.0
$(\alpha_2)_{inj}$ (deg)	0.0	0.0	0.0	0.0

Table 1: Film cooling injection parameters for the EMD configuration

	HPT vane	HPT blade	LPT vane	LPT blade
T_{inj} (R)	1572.9	1588.4	2036.2	1963.6
dW/W_{inlet} (prs)	0.07758	0.07157	0.025215	0.01336
dW/W_{inlet} (sct)	0.03130	0.00800	0.025215	—
$(\alpha_1)_{inj}$ (deg)	10.0	10.0	10.0	10.0
$(\alpha_2)_{inj}$ (deg)	0.0	0.0	0.0	0.0

Table 2: Film cooling injection parameters for the FFR configuration

	HPT vane	HPT blade	LPT vane	LPT blade
$M_{in}(abs)$	0.1125	0.9020	0.6075	0.7181
$M_{in}(rel)$	0.1125	0.3690	0.6075	0.3793
$M_{out}(abs)$	0.9101	0.6347	0.7049	0.4983
$M_{out}(rel)$	0.9101	1.1903	0.7049	0.8515
$\beta_{in}(abs)$	0^o	74.41^o	-44.57^o	-62.62^o
$\beta_{in}(rel)$	0^o	47.73^o	-44.57^o	-29.13^o
$\psi_{in}(abs)$	0^o	-23.41^o	9.56^o	5.18^o
$\psi_{in}(rel)$	0^o	-22.27^o	9.56^o	5.26^o
$\beta_{out}(abs)$	74.82^o	-47.46^o	-63.73^o	33.95^o
$\beta_{out}(rel)$	74.82^o	-68.84^o	-63.73^o	61.09^o
$\psi_{out}(abs)$	6.99^o	2.76^o	-5.31^o	-9.31^o
$\psi_{out}(rel)$	6.99^o	-2.91	-5.31^o	-12.94^o

Table 3: Steady flow quantities at midspan for the EMD configuration, no cooling

	HPT vane	HPT blade	LPT vane	LPT blade
$M_{in}(abs)$	0.1156	0.9052	0.5867	0.7383
$M_{in}(rel)$	0.1156	0.3461	0.5867	0.3672
$M_{out}(abs)$	0.9125	0.6081	0.7348	0.4840
$M_{out}(rel)$	0.9125	1.1865	0.7348	0.8662
$\beta_{in}(abs)$	0^o	75.78^o	-45.33^o	-64.98^o
$\beta_{in}(rel)$	0^o	49.29^o	-45.33^o	-31.82^o
$\psi_{in}(abs)$	0^o	-26.37^o	10.57^o	7.94^o
$\psi_{in}(rel)$	0^o	-8.12^o	10.57^o	0.64^o
$\beta_{out}(abs)$	76.00^o	-47.09^o	-66.01^o	33.65^o
$\beta_{out}(rel)$	76.00^o	-68.80^o	-66.01^o	62.20^o
$\psi_{out}(abs)$	7.18^o	10.59^o	-2.13^o	-12.75^o
$\psi_{out}(rel)$	7.18^o	15.06	-2.13^o	-23.42^o

Table 4: Steady flow quantities at midspan for the EMD configuration, cooling

	HPT vane	HPT blade	LPT vane	LPT blade
$M_{in}(abs)$	0.1154	0.8809	0.6276	0.7281
$M_{in}(rel)$	0.1154	0.3416	0.6276	0.3926
$M_{out}(abs)$	0.8809	0.6276	0.7281	0.5129
$M_{out}(rel)$	0.8809	1.1865	0.7281	0.8453
$\beta_{in}(abs)$	0^o	75.24^o	-39.89^o	-63.27^o
$\beta_{in}(rel)$	0^o	42.88^o	-43.99^o	-32.38^o
$\psi_{in}(abs)$	0^o	-38.83^o	17.08^o	6.15^o
$\psi_{in}(rel)$	0^o	-8.48^o	17.08^o	5.64^o
$\beta_{out}(abs)$	75.24^o	-39.89^o	-63.27^o	31.56^o
$\beta_{out}(rel)$	75.24^o	-69.87^o	-63.27^o	61.36^o
$\psi_{out}(abs)$	-2.16^o	18.40^o	6.55^o	31.50^o
$\psi_{out}(rel)$	-2.16^o	30.48^o	6.55^o	-2.95^o

Table 5: Time-averaged flow quantities at midspan for the EMD configuration, cooling

	HPT vane	HPT blade	LPT vane	LPT blade
$M_{in}(abs)$	0.1205	0.8516	0.5257	0.8949
$M_{in}(rel)$	0.1205	0.2975	0.5257	0.4762
$M_{out}(abs)$	0.8654	0.5357	0.8932	0.5517
$M_{out}(rel)$	0.8654	1.1181	0.8932	0.9632
$\beta_{in}(abs)$	0^o	77.08^o	-42.57^o	-68.62^o
$\beta_{in}(rel)$	0^o	44.97^o	-42.57^o	-44.69^o
$\psi_{in}(abs)$	0^o	-34.98^o	10.45^o	23.59^o
$\psi_{in}(rel)$	0^o	-33.69^o	10.45^o	24.14^o
$\beta_{out}(abs)$	76.72^o	-43.59^o	-69.44^o	36.70^o
$\beta_{out}(rel)$	76.72^o	-69.79^o	-69.44^o	62.73^o
$\psi_{out}(abs)$	23.18^o	-2.25^o	-5.98^o	-6.50^o
$\psi_{out}(rel)$	23.18^o	-9.19	-5.98^o	-11.42^o

Table 6: Steady flow quantities at midspan for the FFR configuration, no cooling

	HPT vane	HPT blade	LPT vane	LPT blade
$M_{in}(abs)$	0.1158	0.8642	0.5193	0.8564
$M_{in}(rel)$	0.1158	0.2938	0.5193	0.4673
$M_{out}(abs)$	0.8631	0.5291	0.8763	0.5603
$M_{out}(rel)$	0.8631	1.1139	0.8763	0.9665
$\beta_{in}(abs)$	0^o	75.77^o	-36.65^o	-68.11^o
$\beta_{in}(rel)$	0^o	38.60^o	-36.65^o	-43.07^o
$\psi_{in}(abs)$	0^o	-5.83^o	9.77^o	28.56^o
$\psi_{in}(rel)$	0^o	-28.69^o	9.77^o	19.66^o
$\beta_{out}(abs)$	75.76^o	-43.45^o	-68.76^o	41.95^o
$\beta_{out}(rel)$	75.76^o	-69.88^o	-68.76^o	64.57^o
$\psi_{out}(abs)$	16.12^o	-2.49^o	-8.35^o	-6.12^o
$\psi_{out}(rel)$	16.12^o	-7.99	-8.35^o	-11.88^o

Table 7: Steady flow quantities at midspan for the FFR configuration, cooling

	HPT vane	HPT blade	LPT vane	LPT blade
$M_{in}(abs)$	0.1158	0.7739	0.5178	0.8636
$M_{in}(rel)$	0.1158	0.2235	0.5178	0.4038
$M_{out}(abs)$	0.7739	0.5178	0.8636	0.5606
$M_{out}(rel)$	0.7739	1.0968	0.8636	0.9635
$\beta_{in}(abs)$	0^o	76.86^o	-34.82^o	-67.76^o
$\beta_{in}(rel)$	0^o	18.00^o	-34.82^o	-43.07^o
$\psi_{in}(abs)$	0^o	-40.38^o	10.60^o	-36.01^o
$\psi_{in}(rel)$	0^o	-33.73^o	10.60^o	1.64^o
$\beta_{out}(abs)$	76.86^o	-34.82^o	-67.76^o	37.39^o
$\beta_{out}(rel)$	76.86^o	-65.02^o	-67.76^o	63.33^o
$\psi_{out}(abs)$	-40.38^o	10.60^o	-36.01^o	9.12^o
$\psi_{out}(rel)$	-40.38^o	57.87	-36.01^o	24.24^o

Table 8: Time-averaged flow quantities at midspan for the FFR configuration, cooling

	HPT Stage	LPT Stage
EMD (Steady, no cooling)	0.813	0.763
EMD (Steady, cooling)	0.797	0.788
EMD (Unsteady, cooling)	0.845	0.729
FFR (Steady, no cooling)	0.858	0.804
FFR (Steady, cooling)	0.869	0.834
FFR (Unsteady, cooling)	0.928	0.756

Table 9: Efficiencies of the HPT and LPT stages in the steady/unsteady simulations

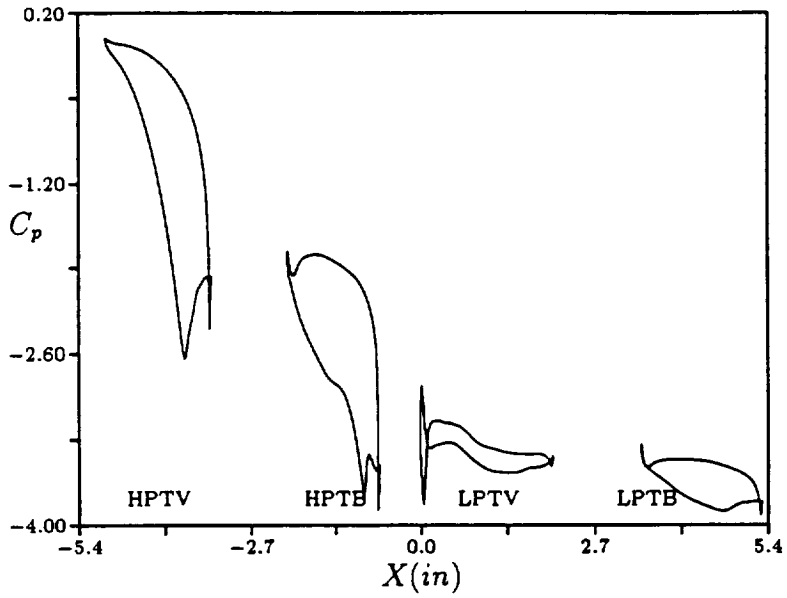

Figure 1: Time-averaged surface pressure coefficient distributions at 10% span - EMD

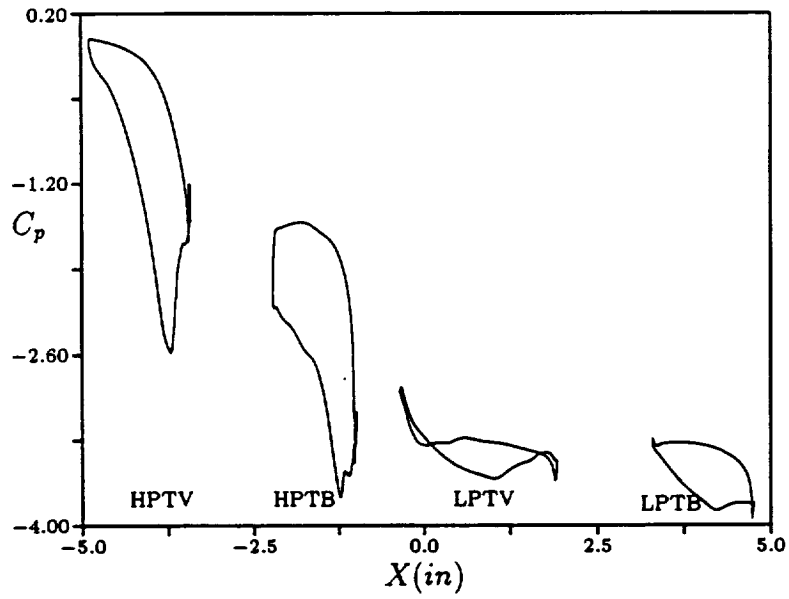

Figure 2: Time-averaged surface pressure coefficient distributions at 50% span - EMD

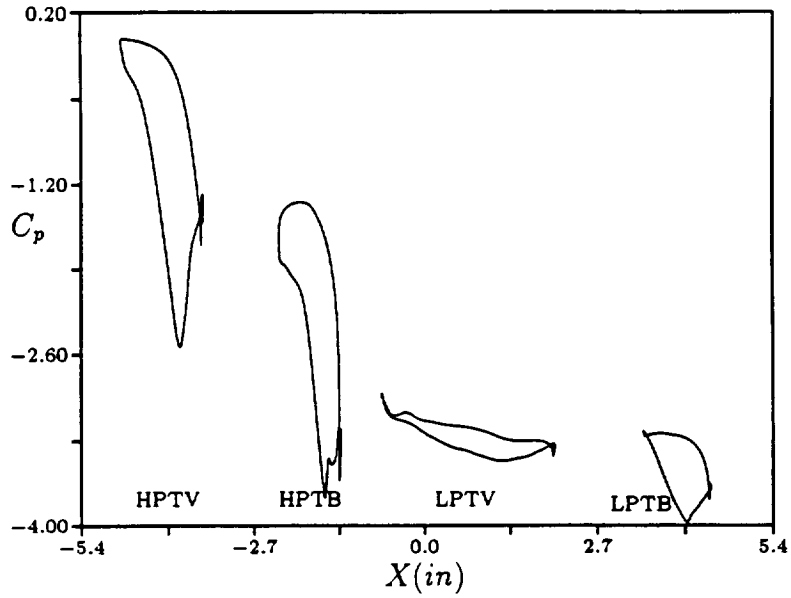

Figure 3: Time-averaged surface pressure coefficient distributions at 90% span - EMD

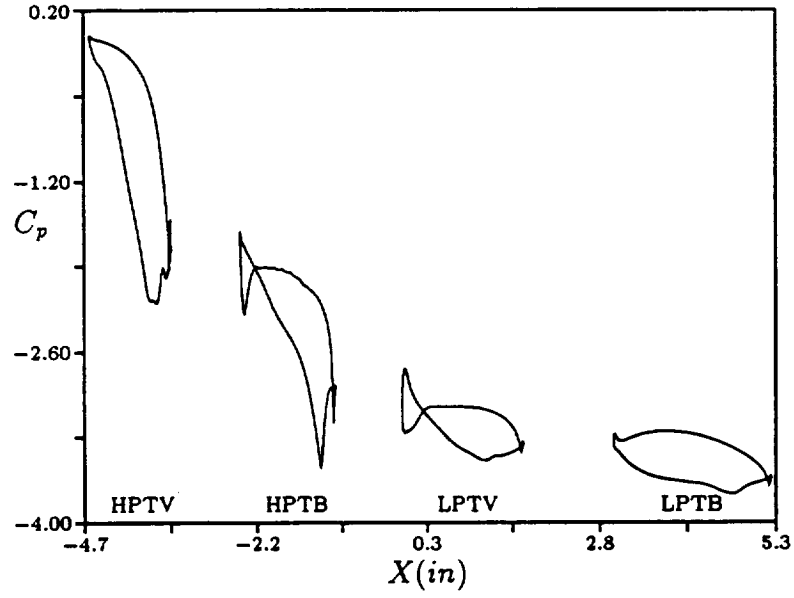

Figure 4: Time-averaged surface pressure coefficient distributions at 10% span - FFR

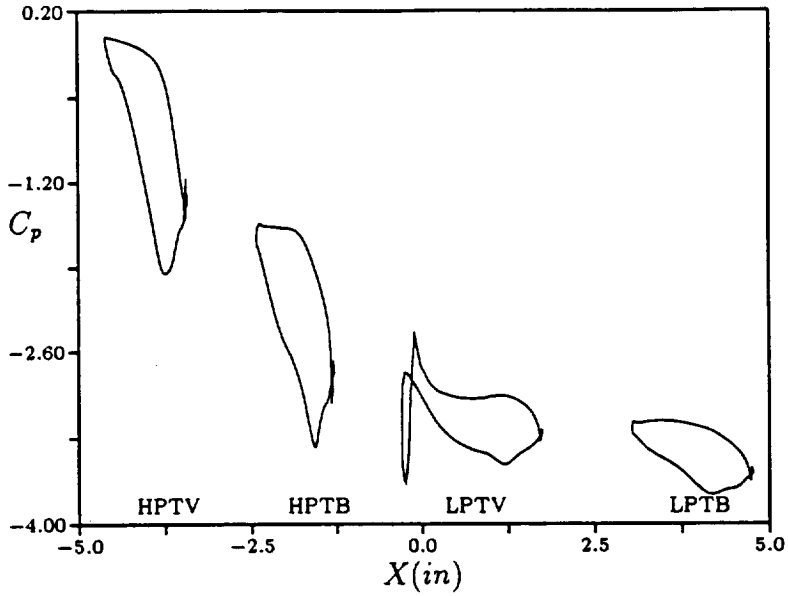

Figure 5: Time-averaged surface pressure coefficient distributions at 50% span - FFR

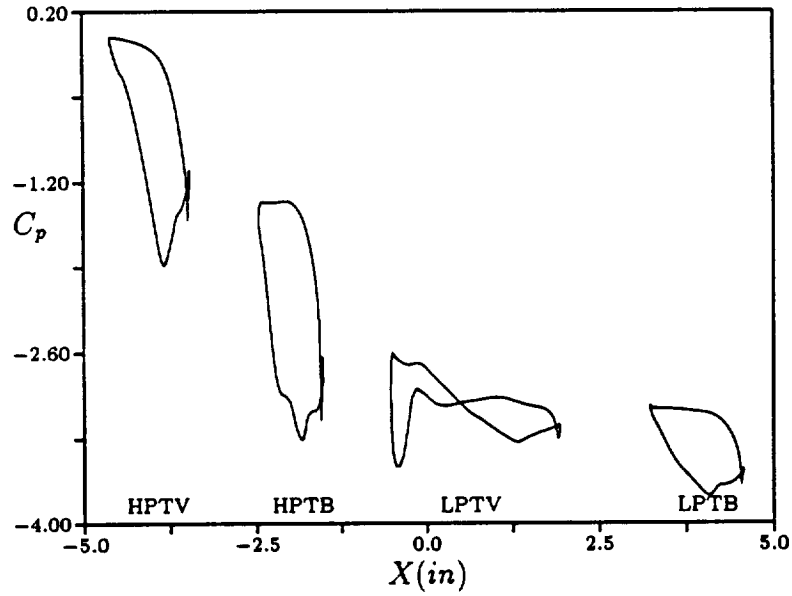

Figure 6: Time-averaged surface pressure coefficient distributions at 90% span - FFR

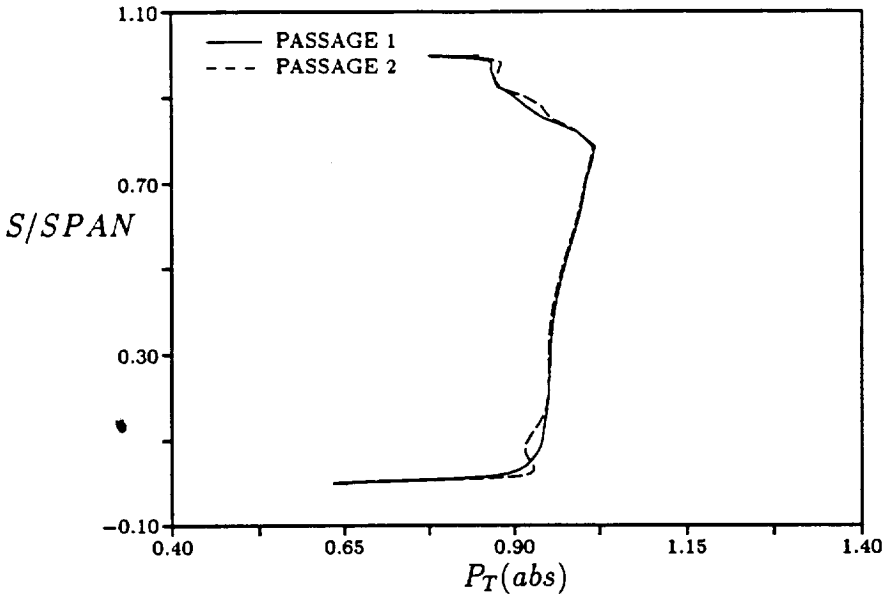

Figure 7: Absolute total pressure distribution at the HPT vane exit - EMD

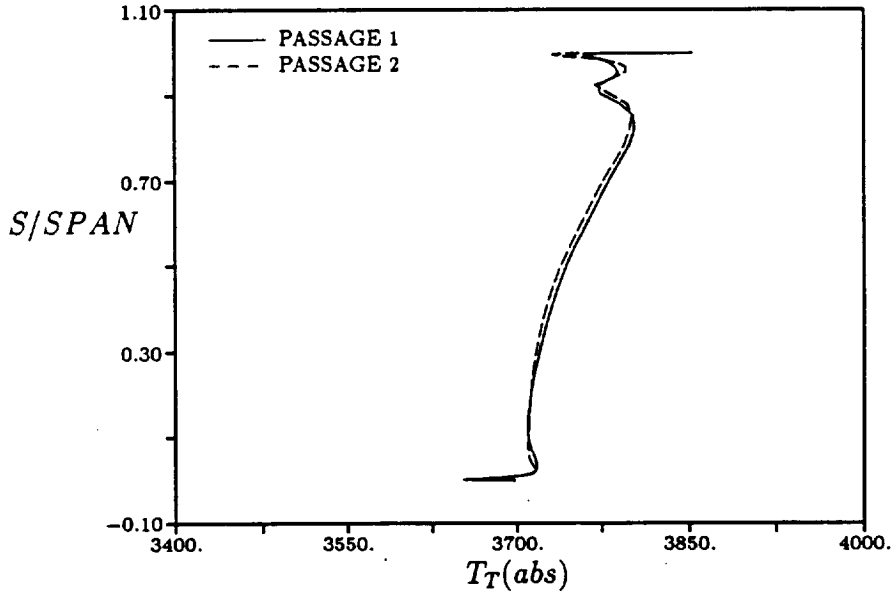

Figure 8: Absolute total temperature distribution at the HPT vane exit - EMD

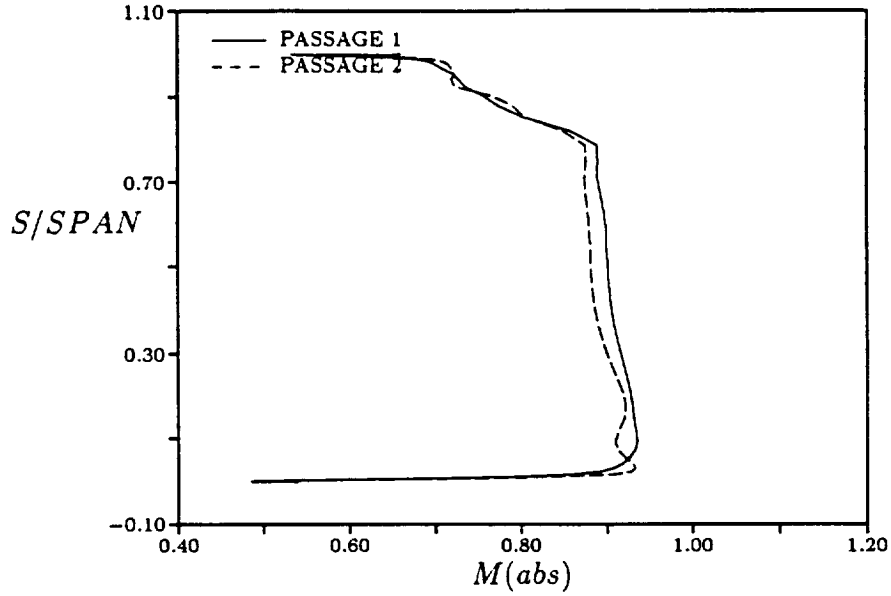

Figure 9: Absolute Mach number distribution at the HPT vane exit - EMD

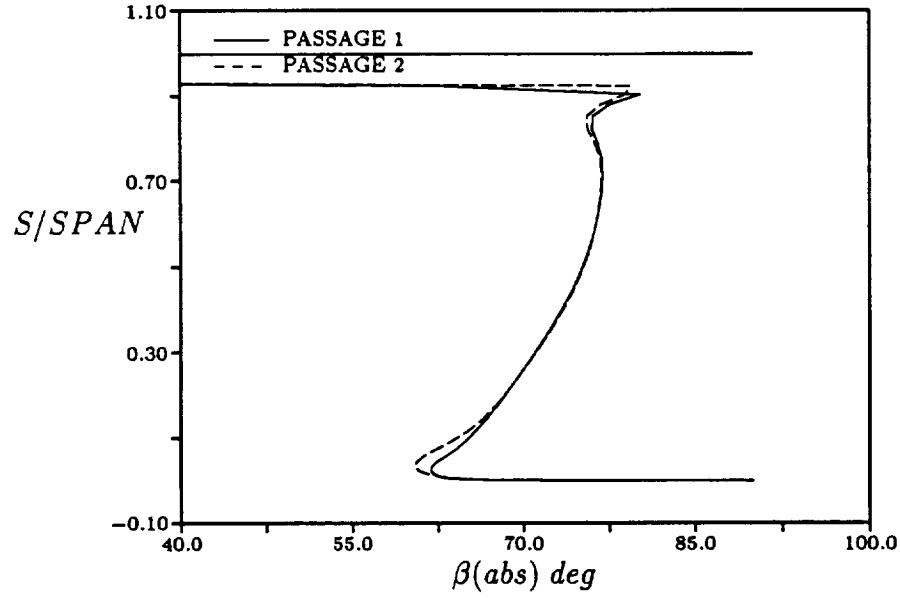

Figure 10: Absolute flow pitch angle distribution at the HPT vane exit - EMD

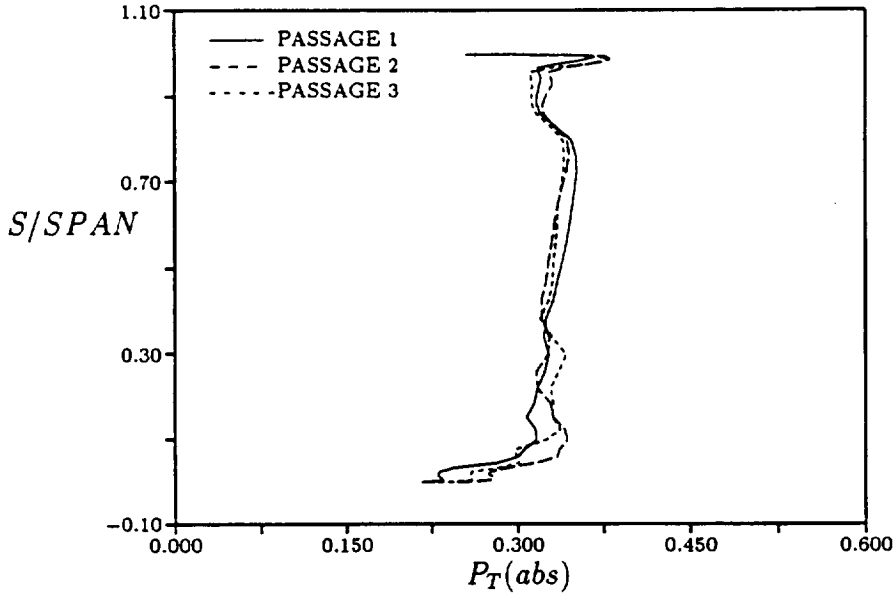

Figure 11: Absolute total pressure distribution at the HPT blade exit - EMD

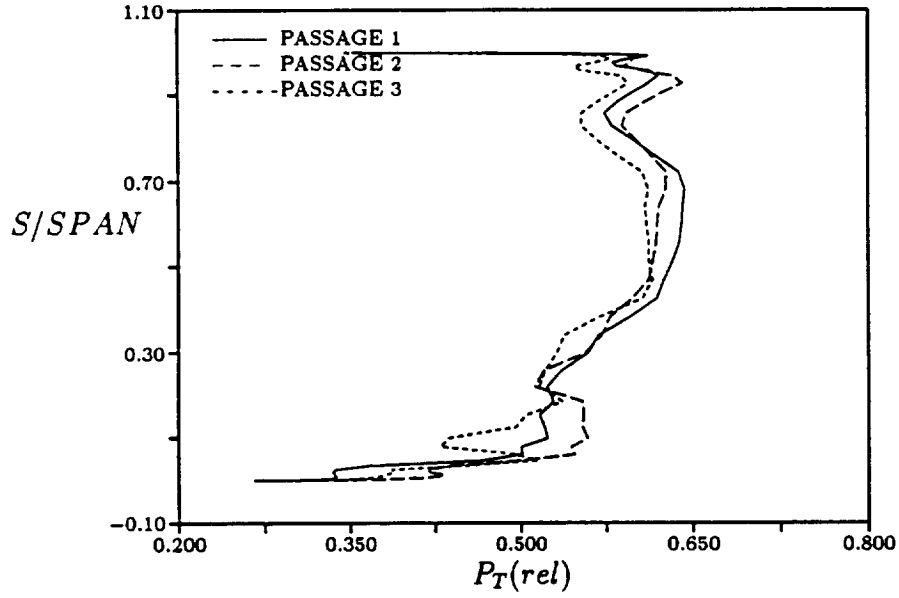

Figure 12: Relative total pressure distribution at the HPT blade exit - EMD

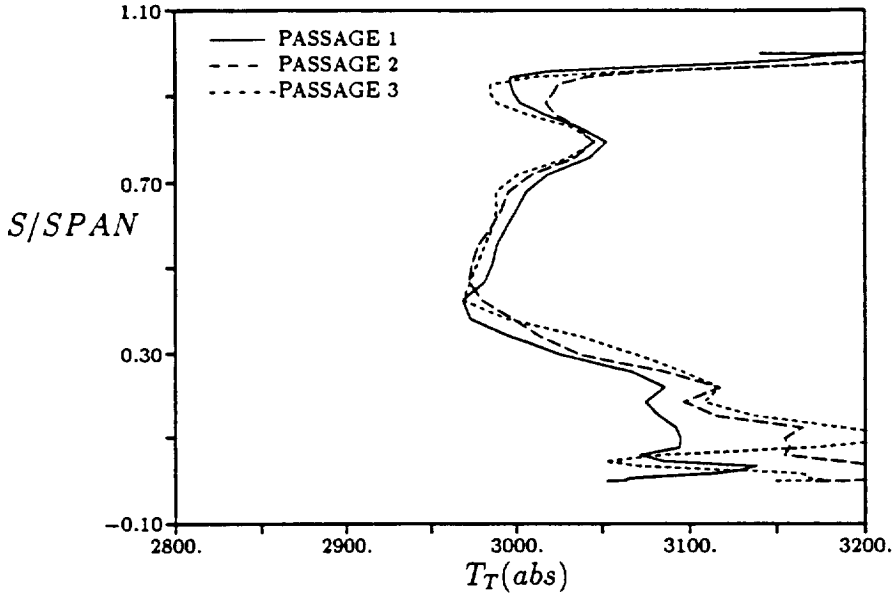

Figure 13: Absolute total temperature distribution at the HPT blade exit - EMD

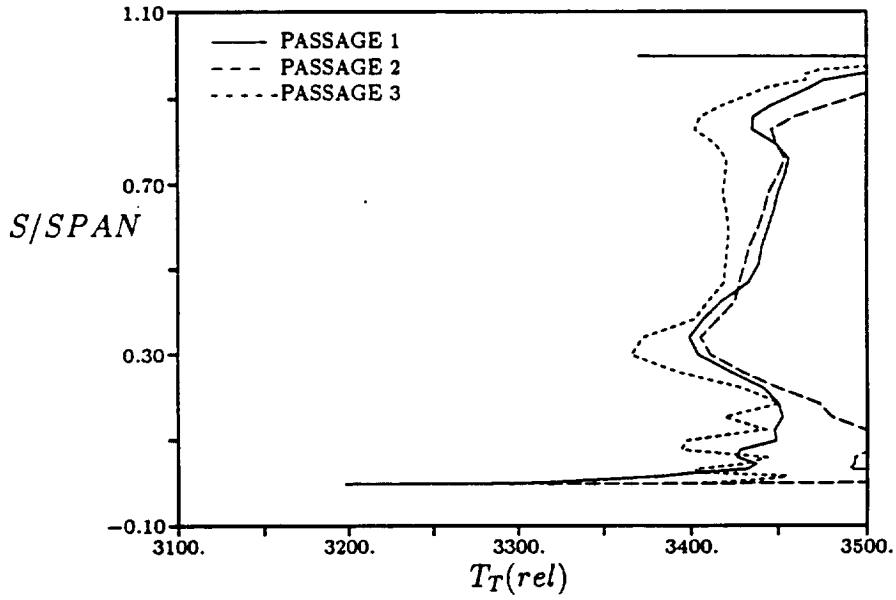

Figure 14: Relative total temperature distribution at the HPT blade exit - EMD

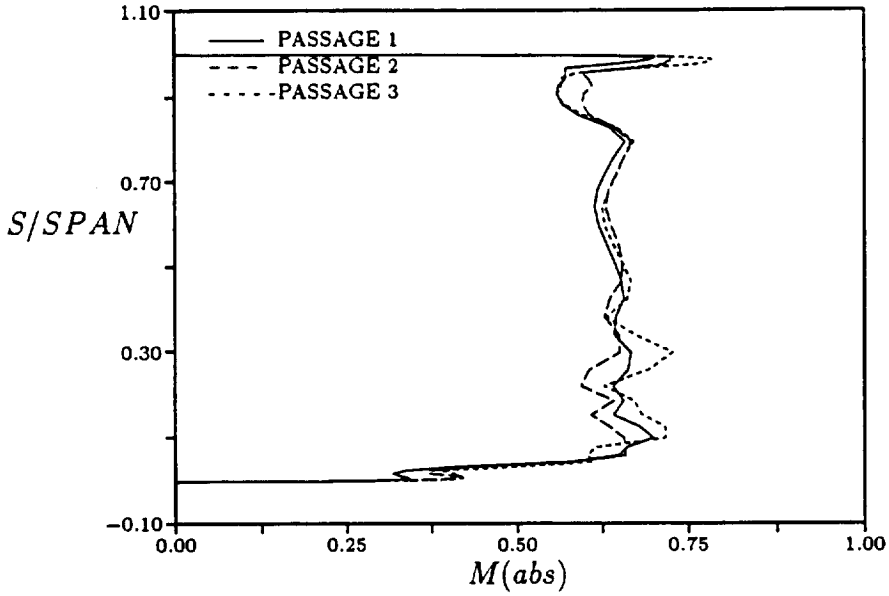

Figure 15: Absolute Mach number distribution at the HPT blade exit - EMD

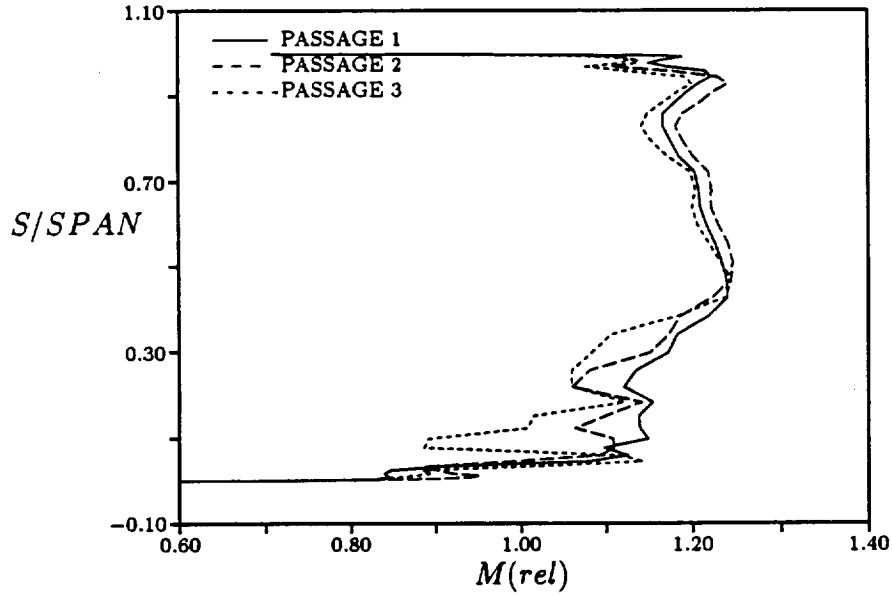

Figure 16: Relative Mach number distribution at the HPT blade exit - EMD

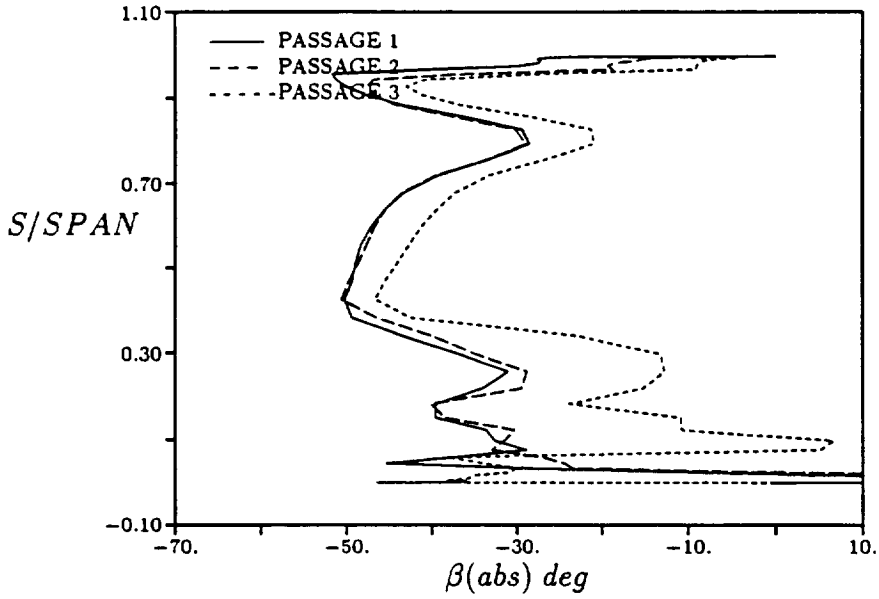

Figure 17: Absolute flow pitch angle distribution at the HPT blade exit - EMD

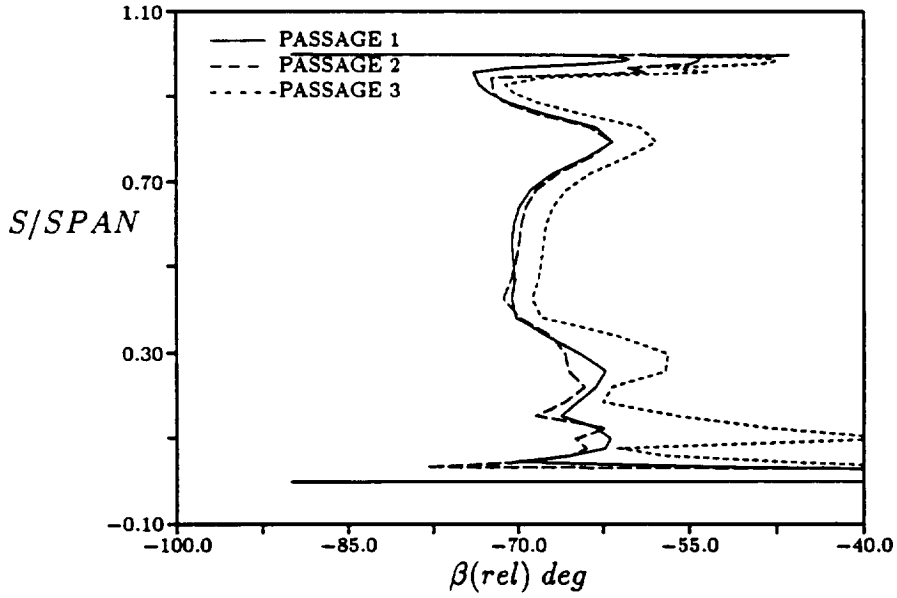

Figure 18: Relative flow pitch angle distribution at the HPT blade exit - EMD

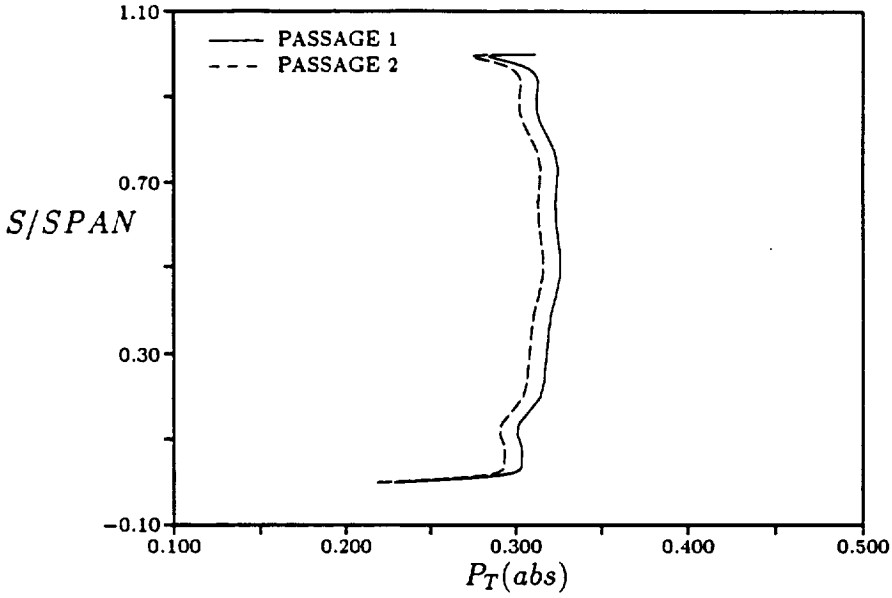

Figure 19: Absolute total pressure distribution at the LPT vane exit - EMD

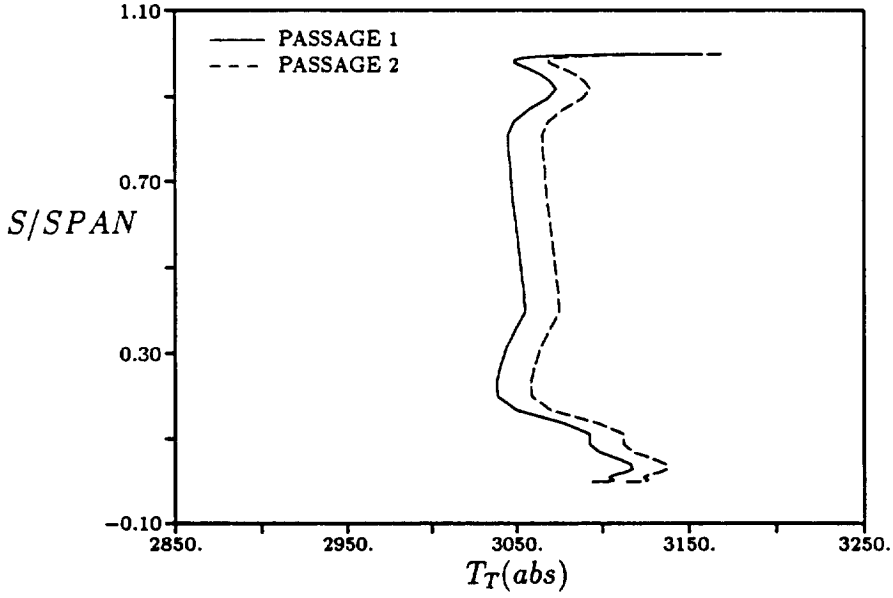

Figure 20: Absolute total temperature distribution at the LPT vane exit - EMD

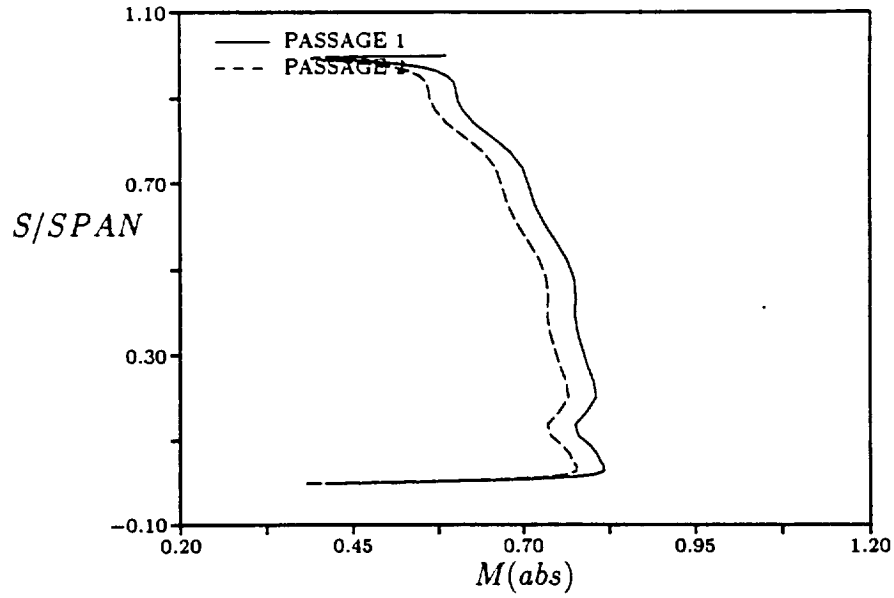

Figure 21: Absolute Mach number distribution at the LPT vane exit - EMD

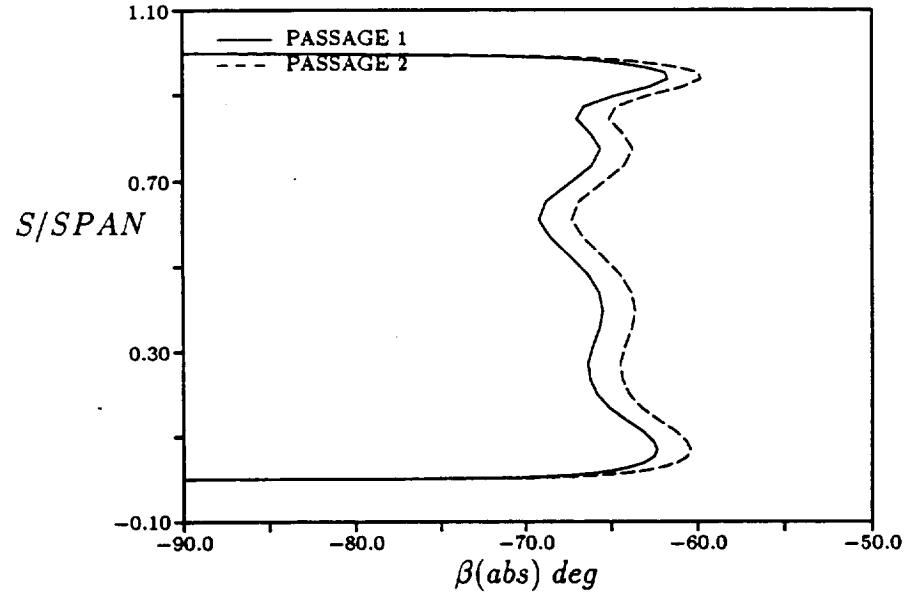

Figure 22: Absolute flow pitch angle distribution at the LPT vane exit - EMD

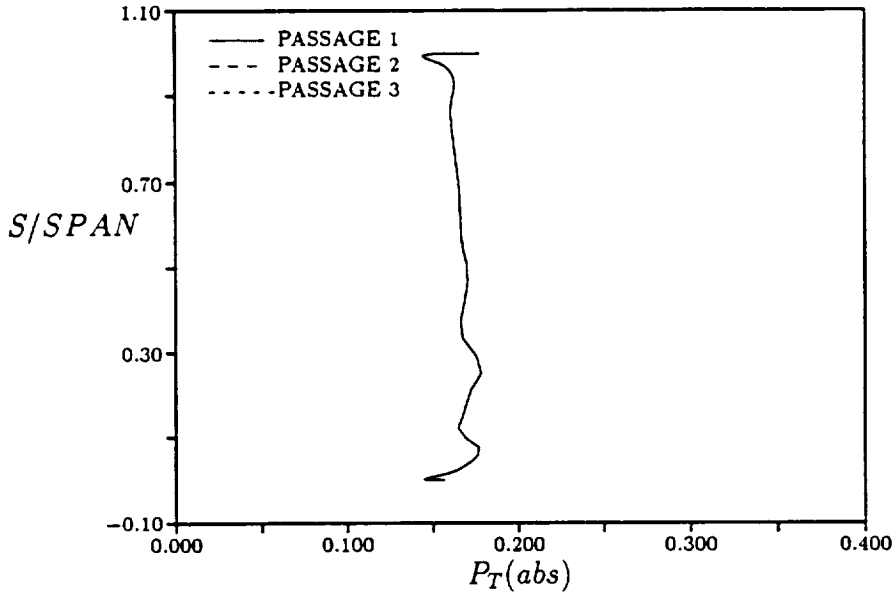

Figure 23: Absolute total pressure distribution at the LPT blade exit - EMD

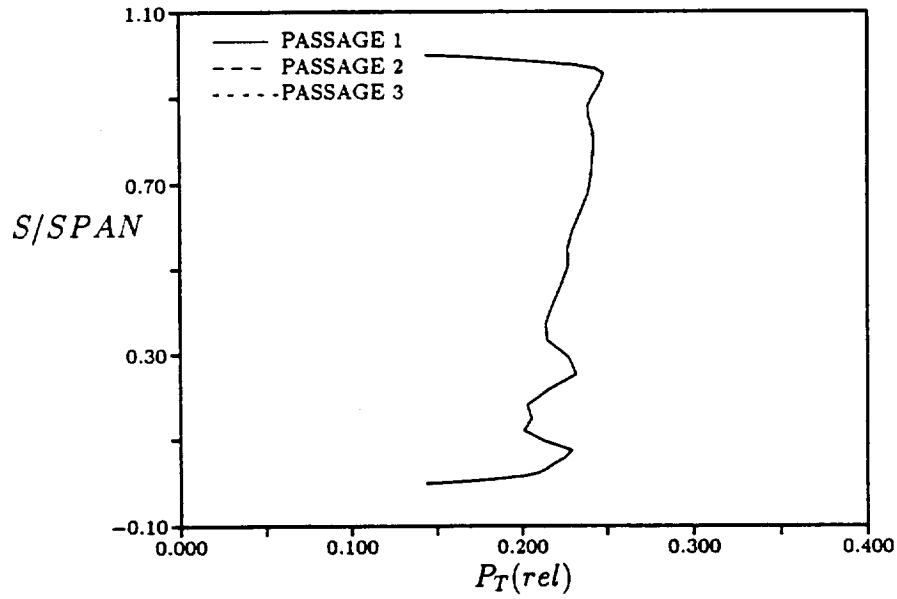

Figure 24: Relative total pressure distribution at the LPT blade exit - EMD

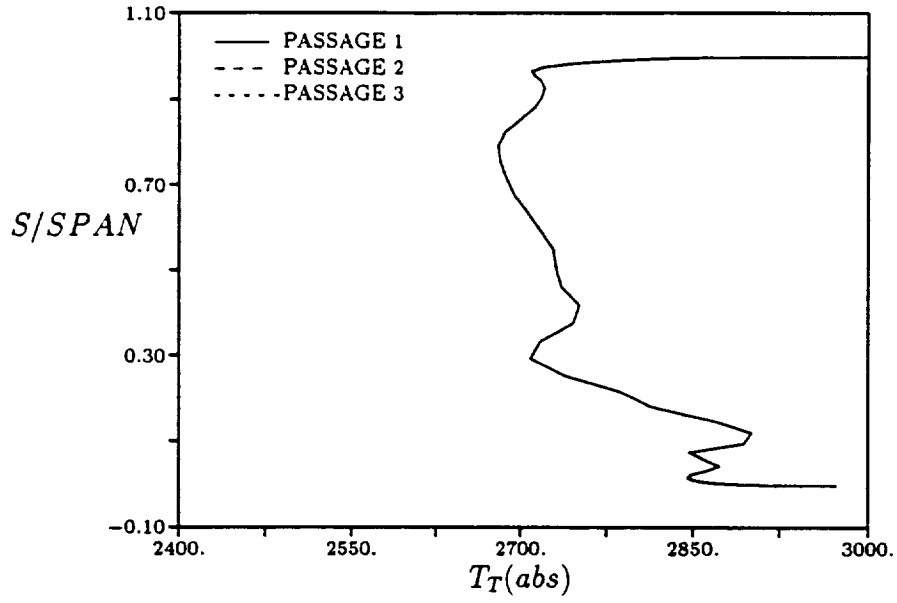

Figure 25: Absolute total temperature distribution at the LPT blade exit - EMD

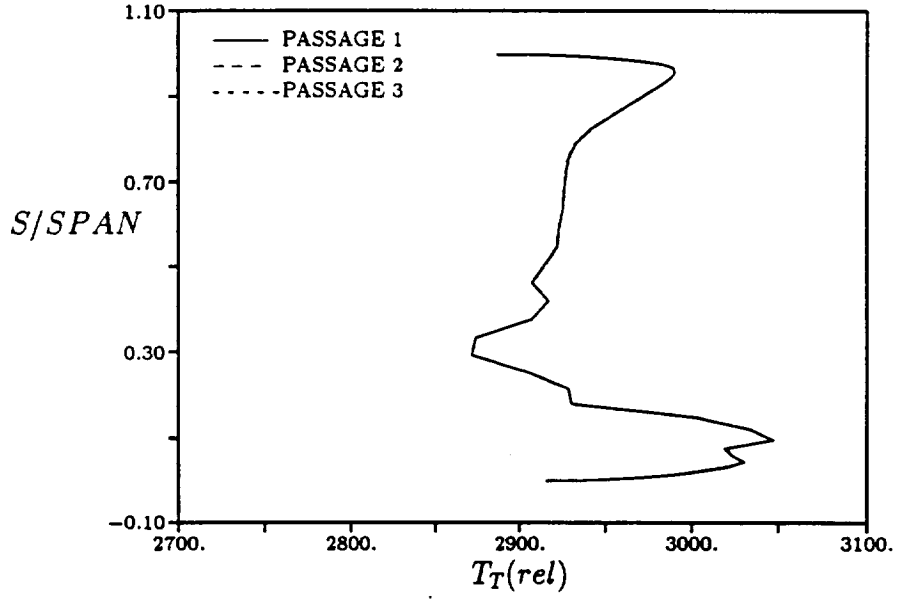

Figure 26: Relative total temperature distribution at the LPT blade exit - EMD

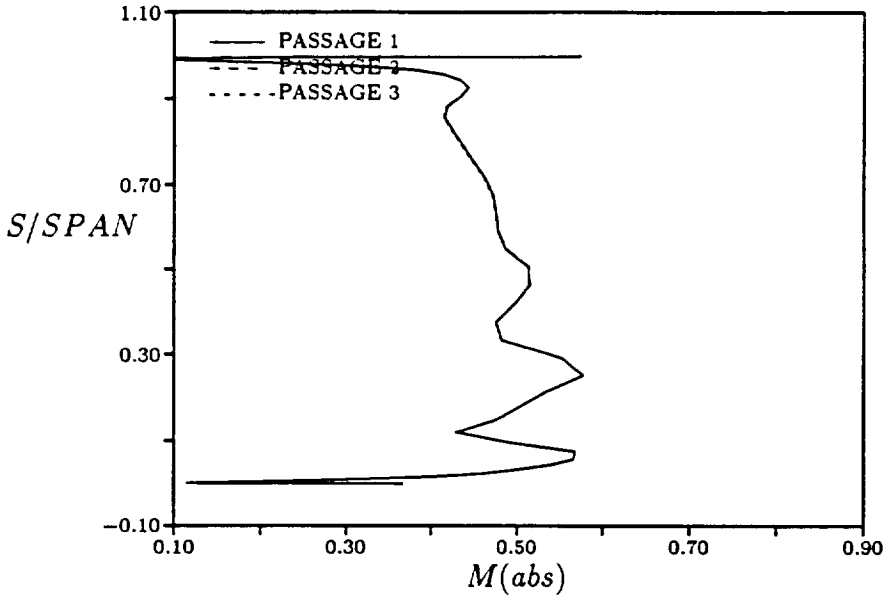

Figure 27: Absolute Mach number distribution at the LPT blade exit - EMD

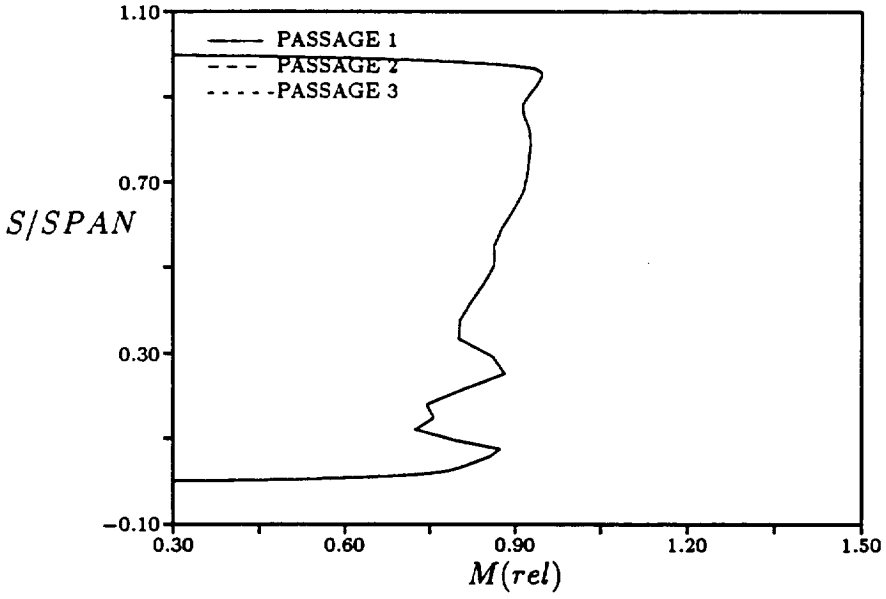

Figure 28: Relative Mach number distribution at the LPT blade exit - EMD

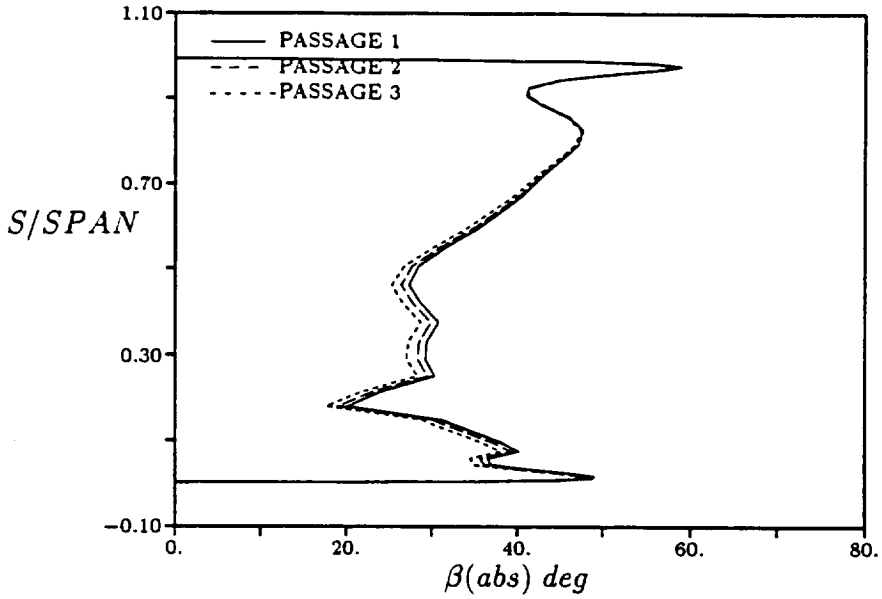

Figure 29: Absolute flow pitch angle distribution at the LPT blade exit - EMD

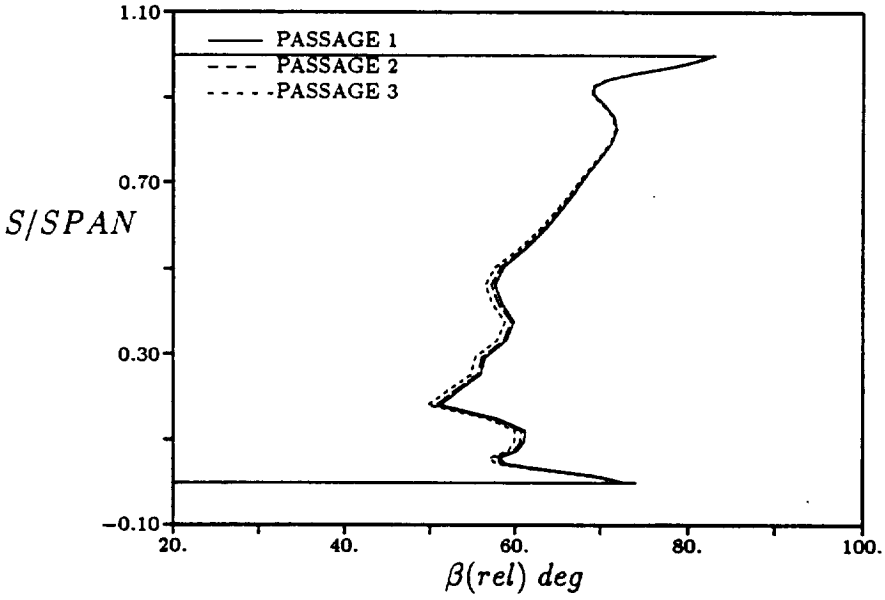

Figure 30: Relative flow pitch angle distribution at the LPT blade exit - EMD

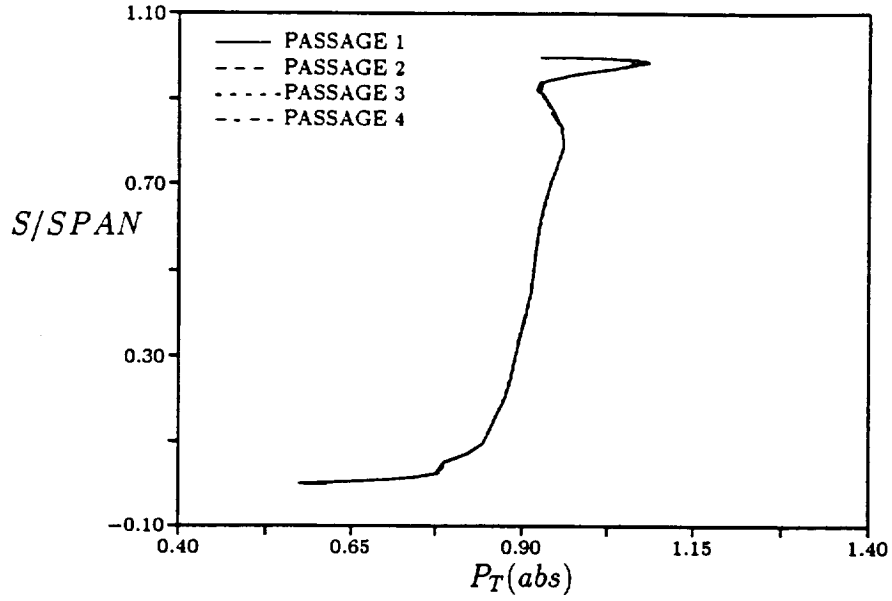

Figure 31: Absolute total pressure distribution at the HPT vane exit - FFR

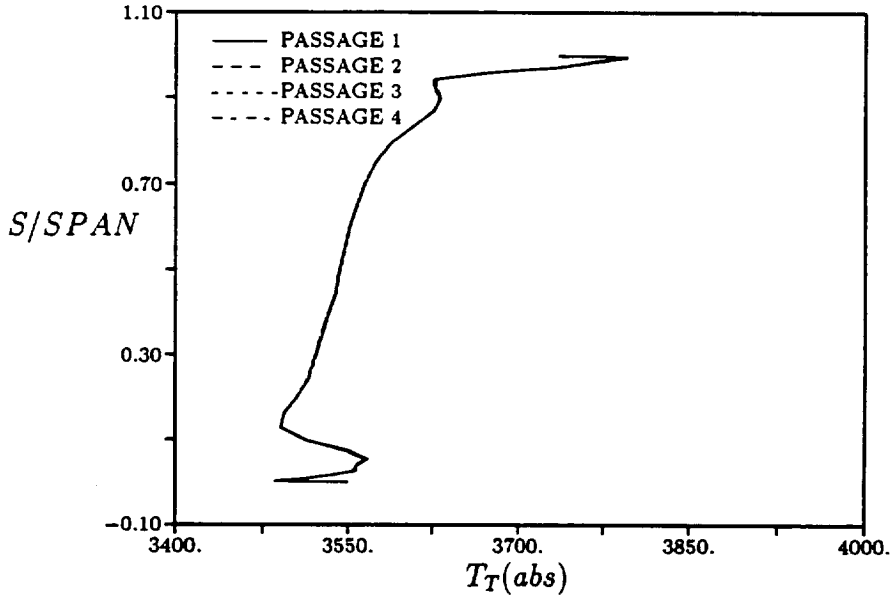

Figure 32: Absolute total temperature distribution at the HPT vane exit - FFR

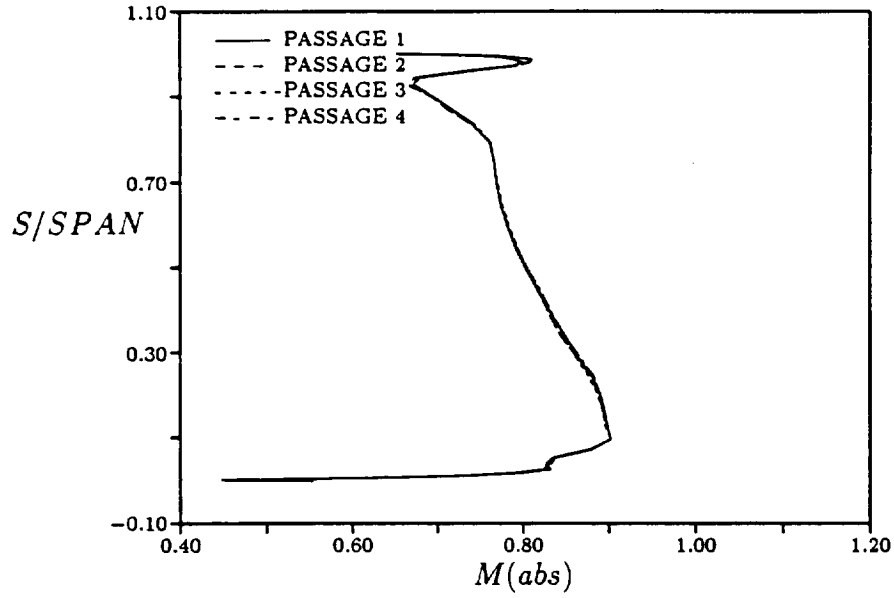

Figure 33: Absolute Mach number distribution at the HPT vane exit - FFR

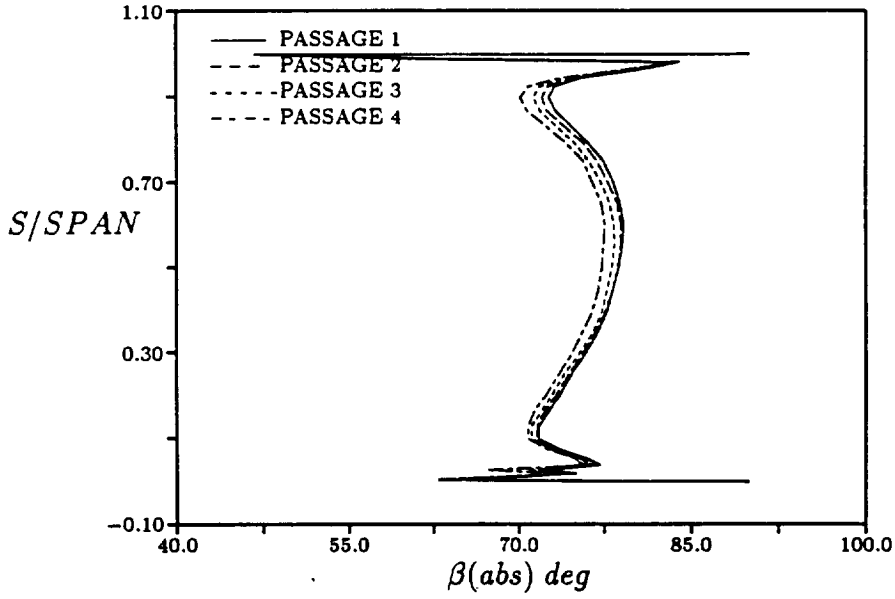

Figure 34: Absolute flow pitch angle distribution at the HPT vane exit - FFR

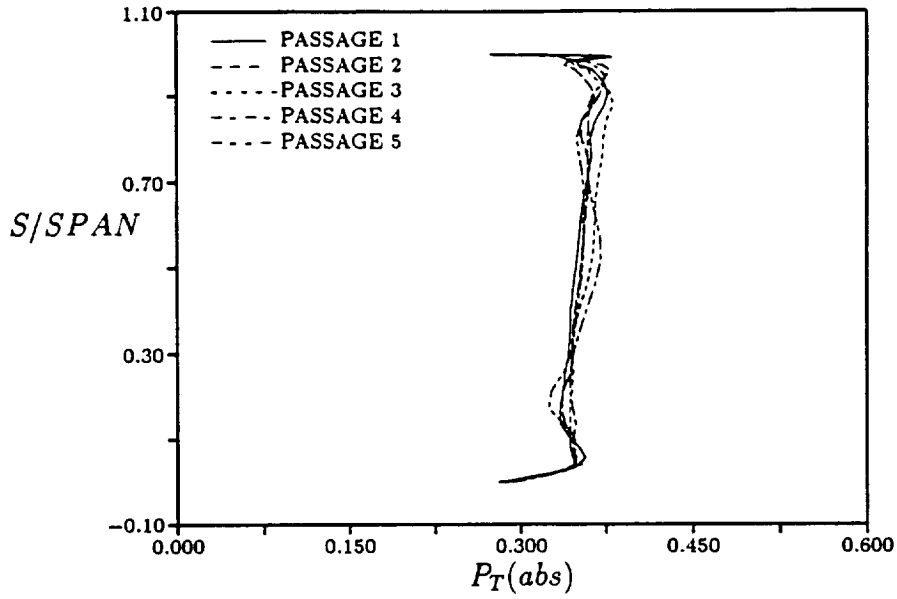

Figure 35: Absolute total pressure distribution at the HPT blade exit - FFR

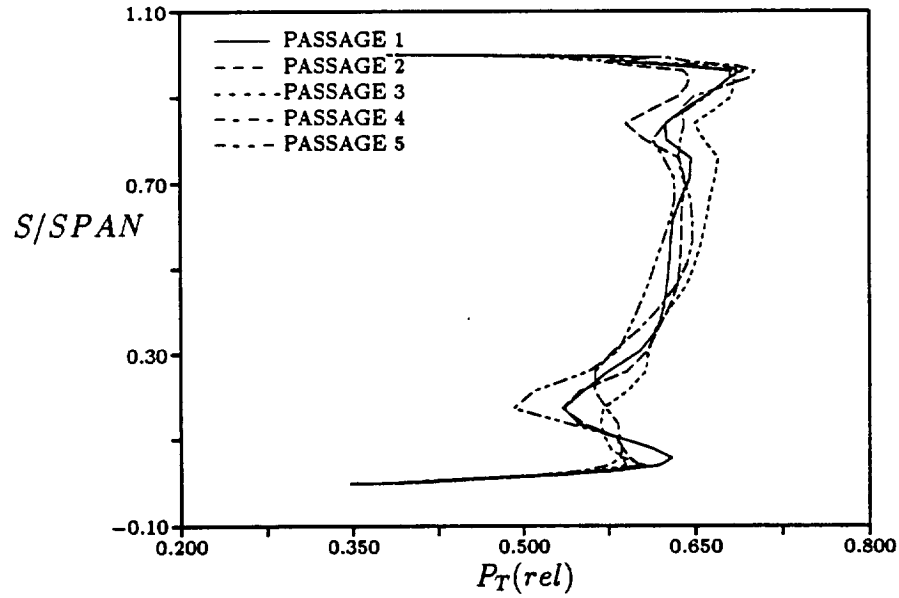

Figure 36: Relative total pressure distribution at the HPT blade exit - FFR

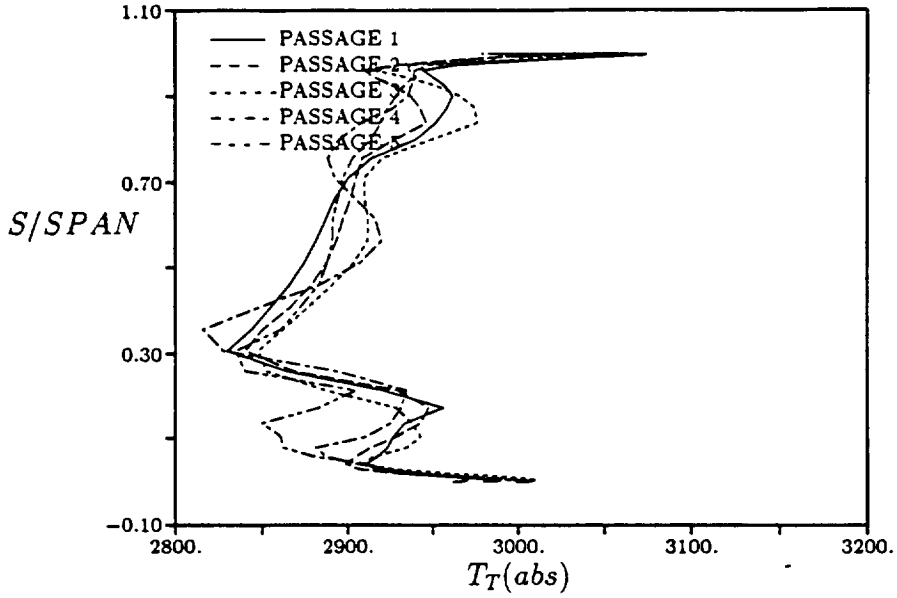

Figure 37: Absolute total temperature distribution at the HPT blade exit - FFR

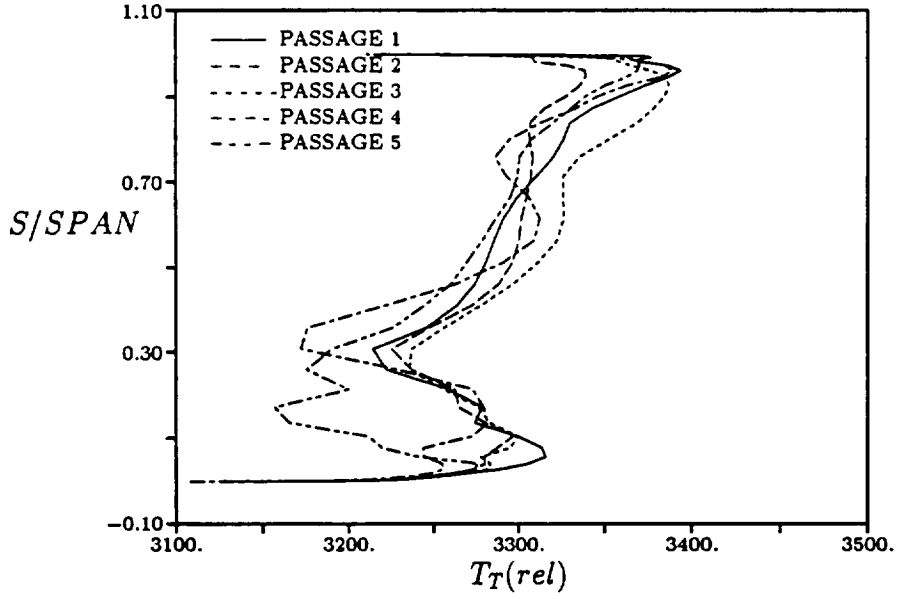

Figure 38: Relative total temperature distribution at the HPT blade exit - FFR

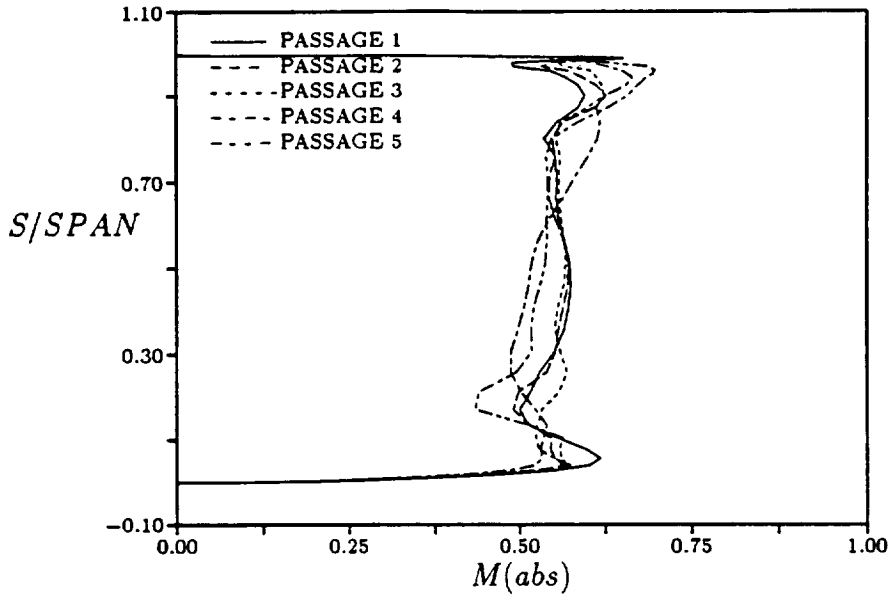

Figure 39: Absolute Mach number distribution at the HPT blade exit - FFR

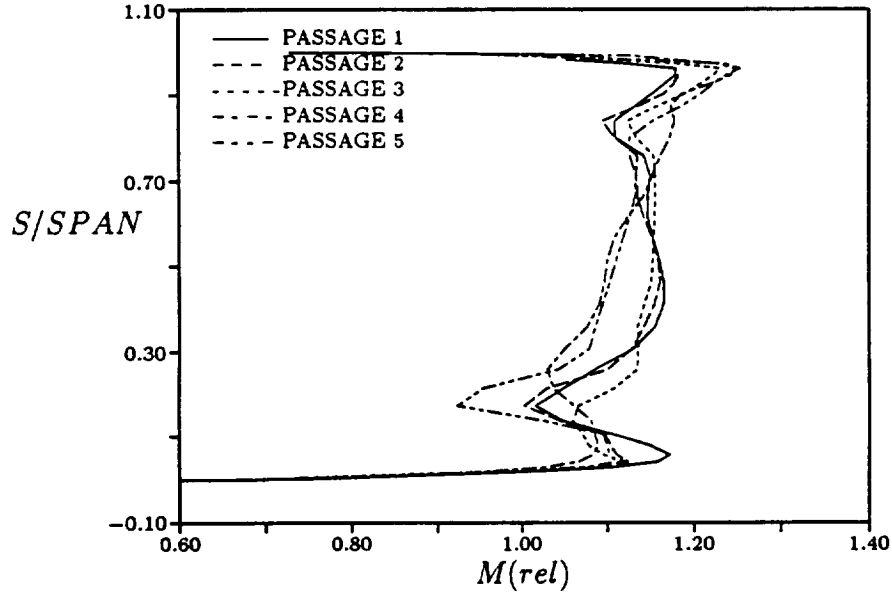

Figure 40: Relative Mach number distribution at the HPT blade exit - FFR

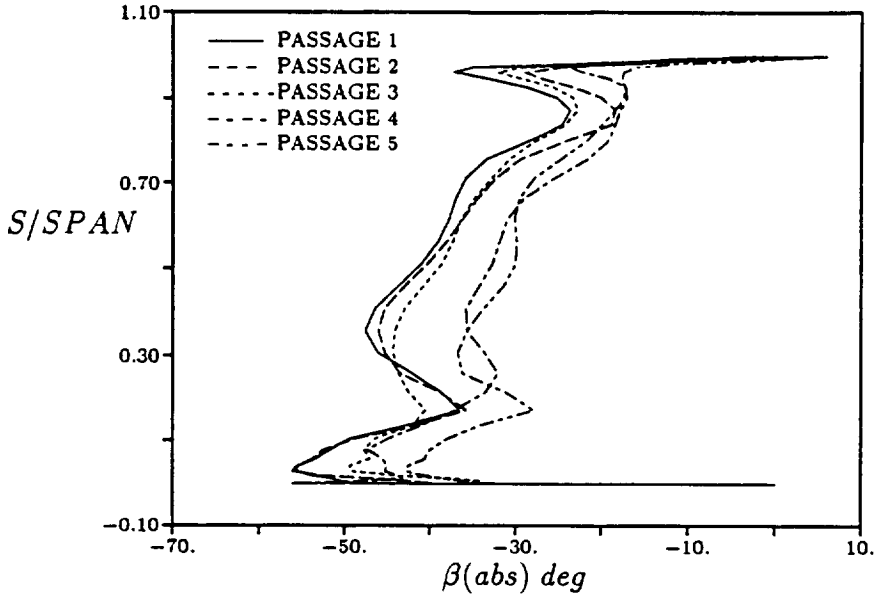

Figure 41: Absolute flow pitch angle distribution at the HPT blade exit - FFR

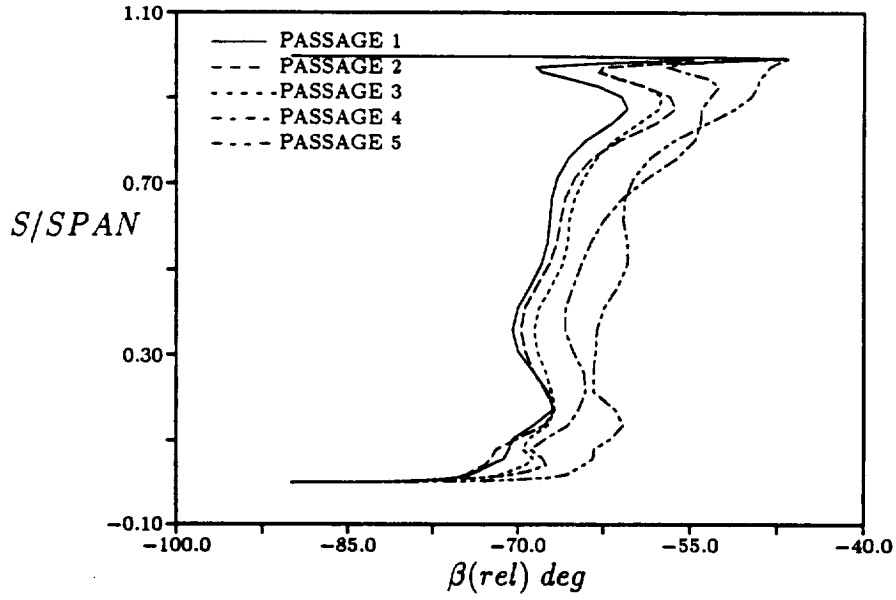

Figure 42: Relative flow pitch angle distribution at the HPT blade exit - FFR

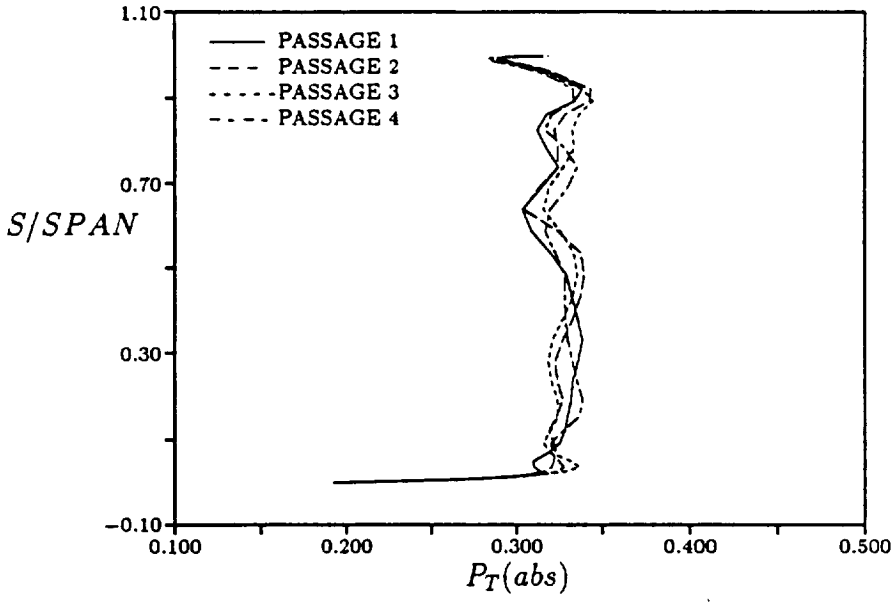

Figure 43: Absolute total pressure distribution at the LPT vane exit - FFR

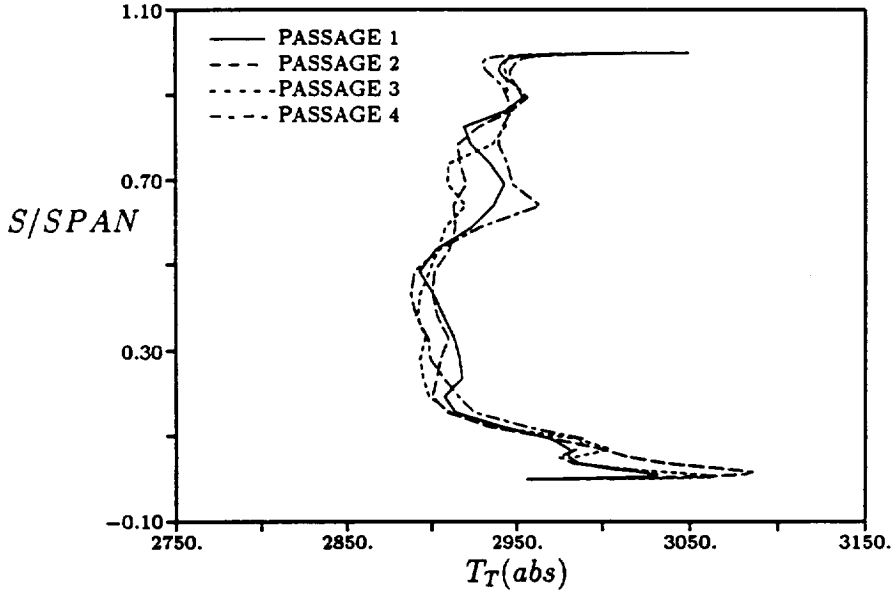

Figure 44: Absolute total temperature distribution at the LPT vane exit - FFR

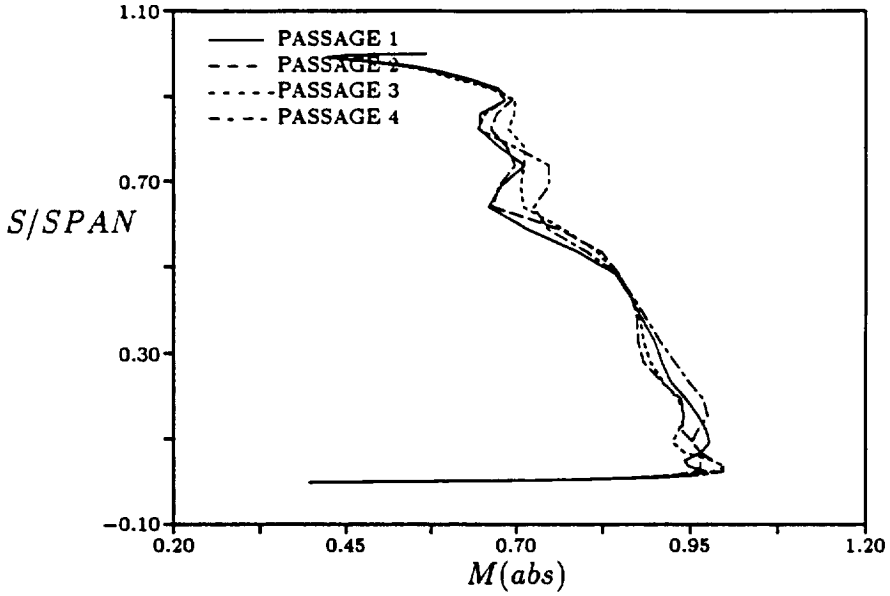

Figure 45: Absolute Mach number distribution at the LPT vane exit - FFR

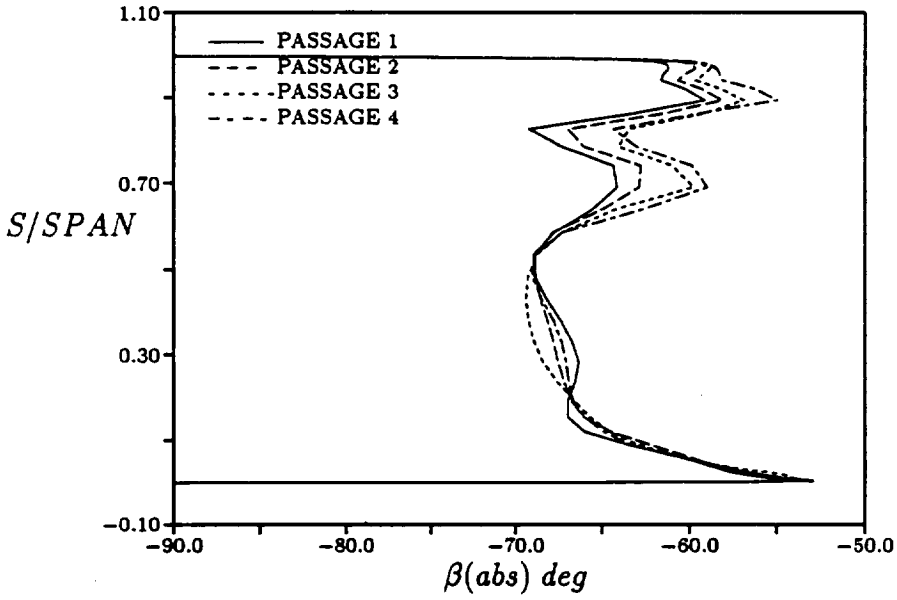

Figure 46: Absolute flow pitch angle distribution at the LPT vane exit - FFR

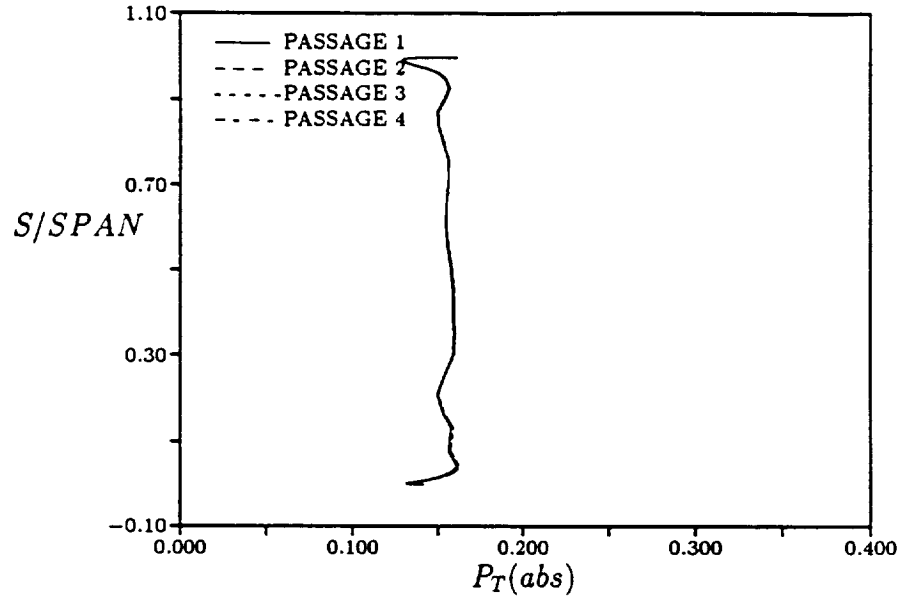

Figure 47: Absolute total pressure distribution at the LPT blade exit - FFR

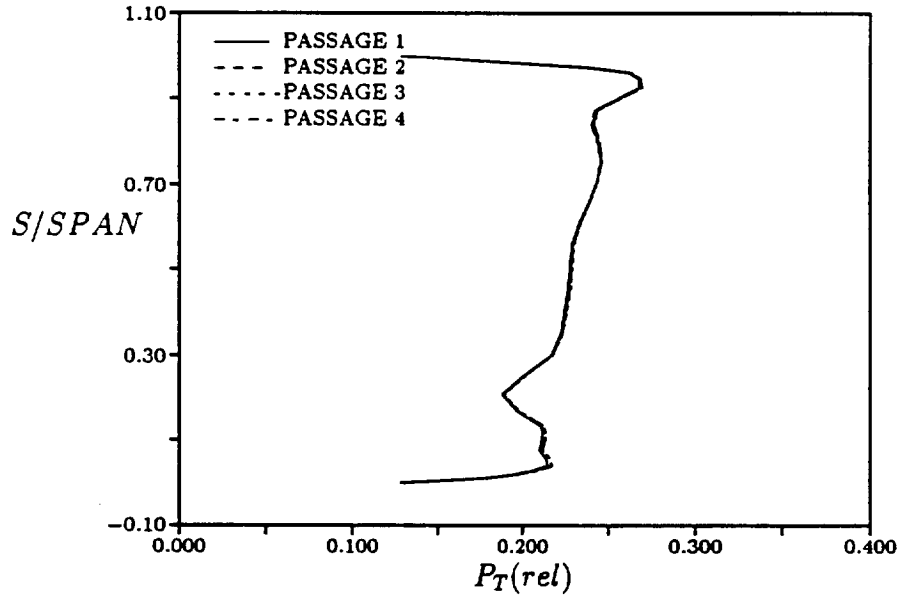

Figure 48: Relative total pressure distribution at the LPT blade exit - FFR

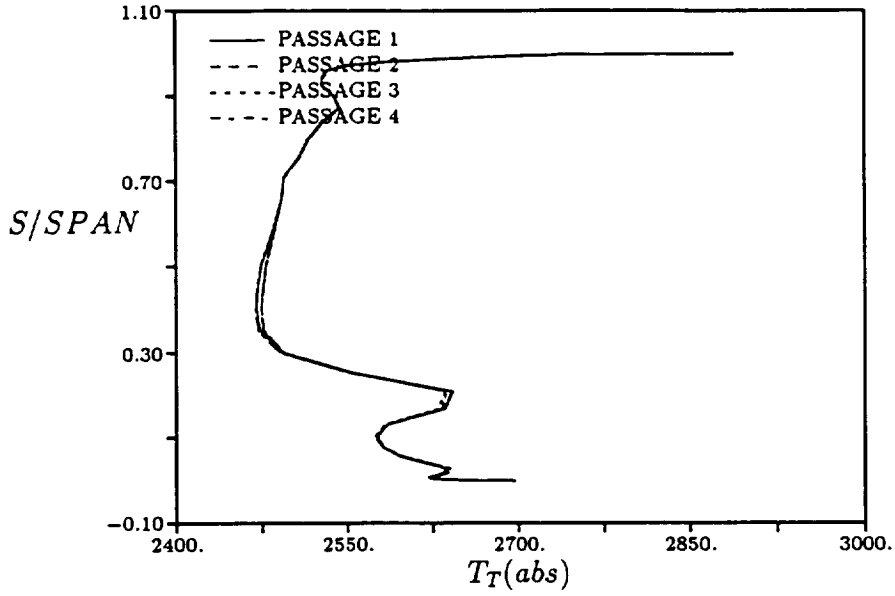

Figure 49: Absolute total temperature distribution at the LPT blade exit - FFR

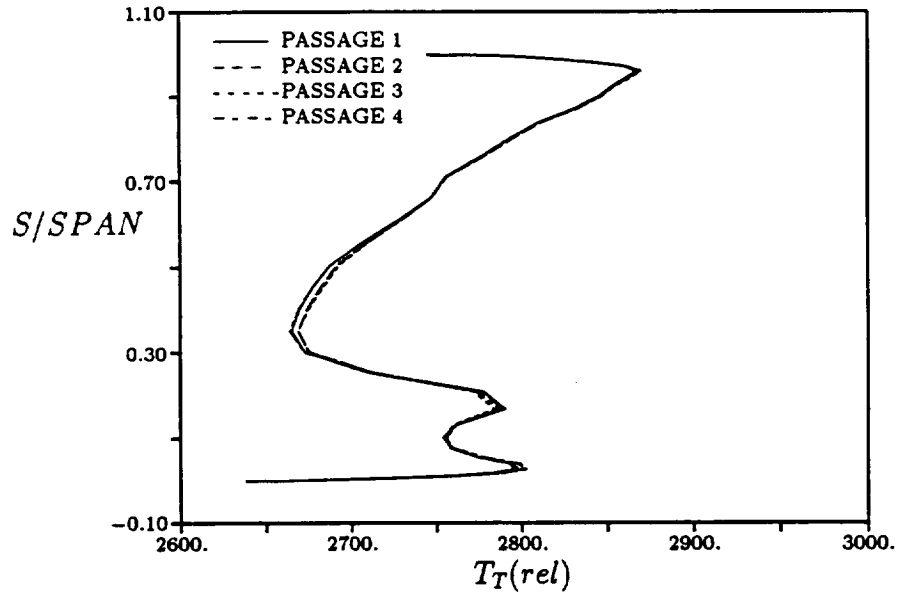

Figure 50: Relative total temperature distribution at the LPT blade exit - FFR

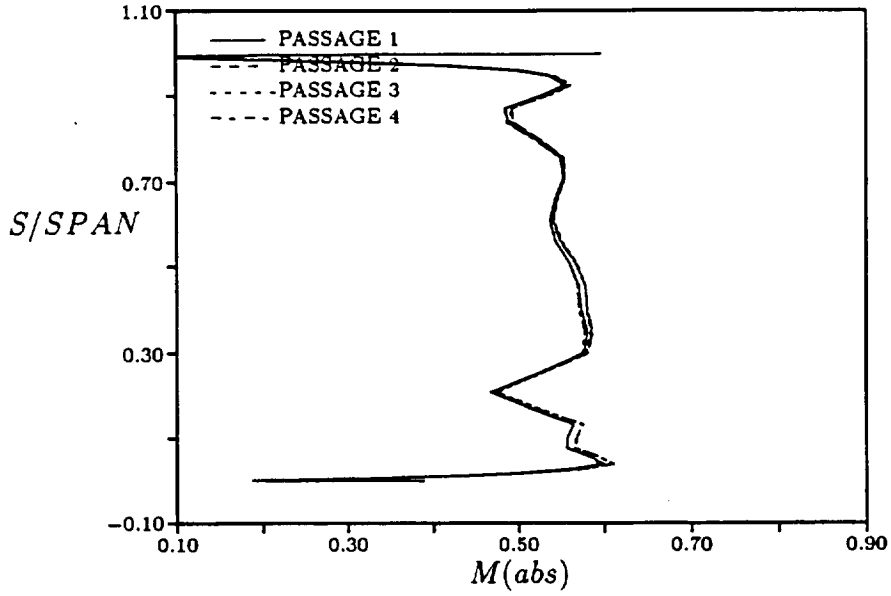

Figure 51: Absolute Mach number distribution at the LPT blade exit - FFR

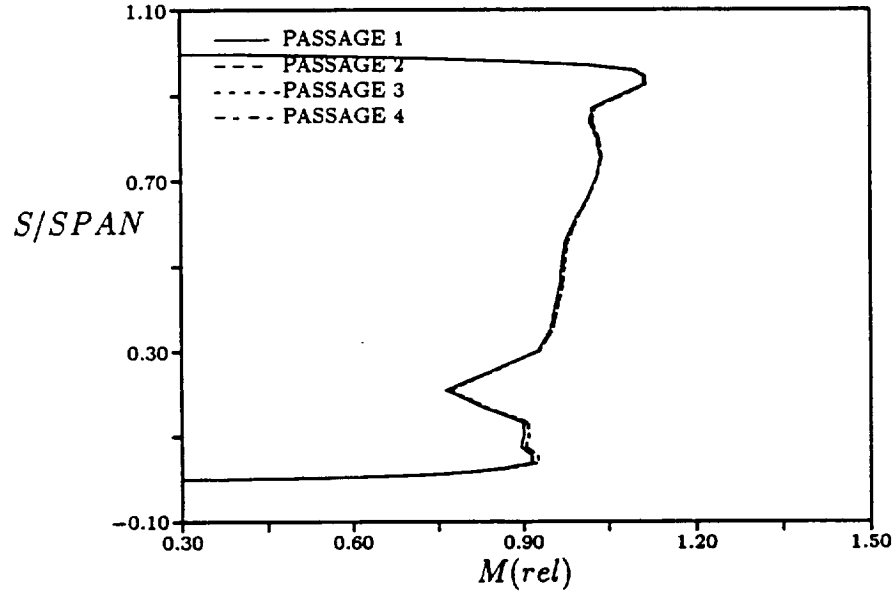

Figure 52: Relative Mach number distribution at the LPT blade exit - FFR

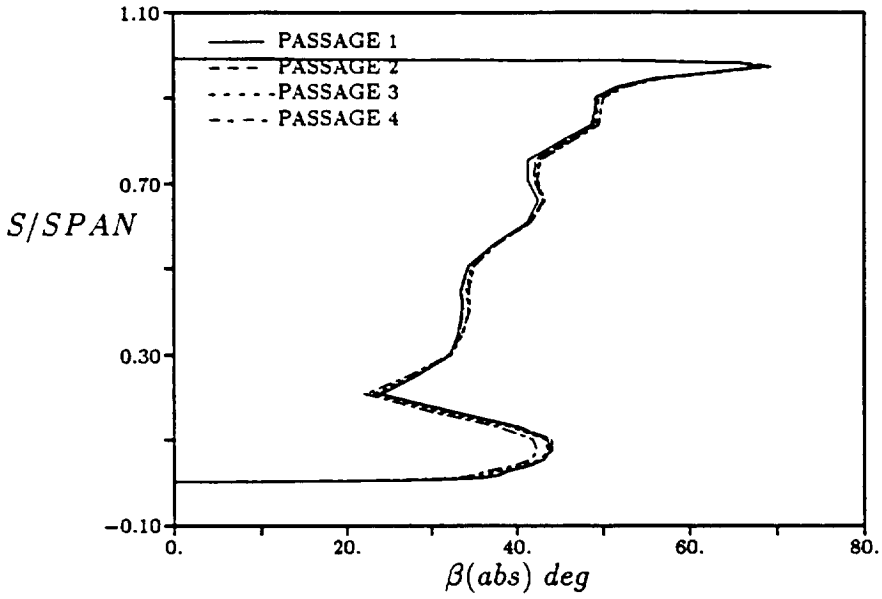

Figure 53: Absolute flow pitch angle distribution at the LPT blade exit - FFR

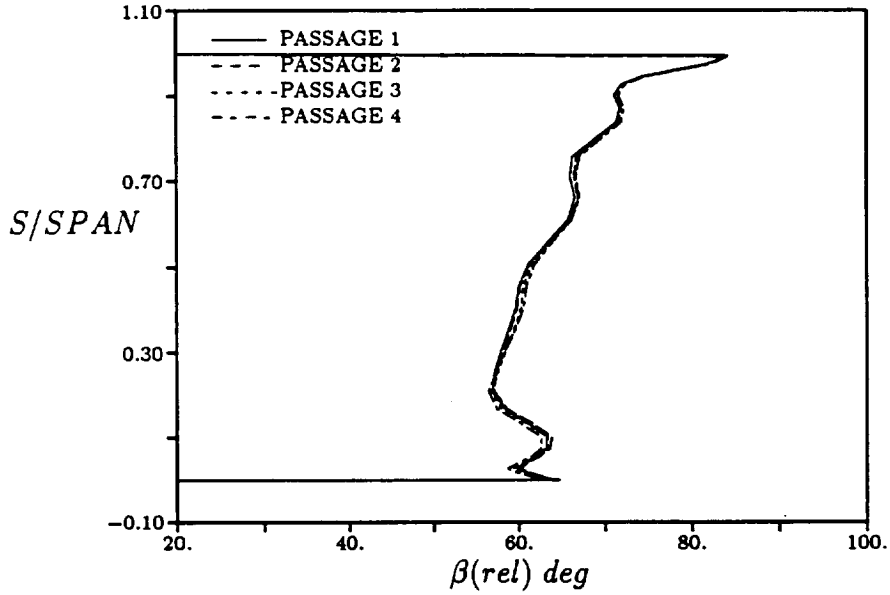

Figure 54: Relative flow pitch angle distribution at the LPT blade exit - FFR

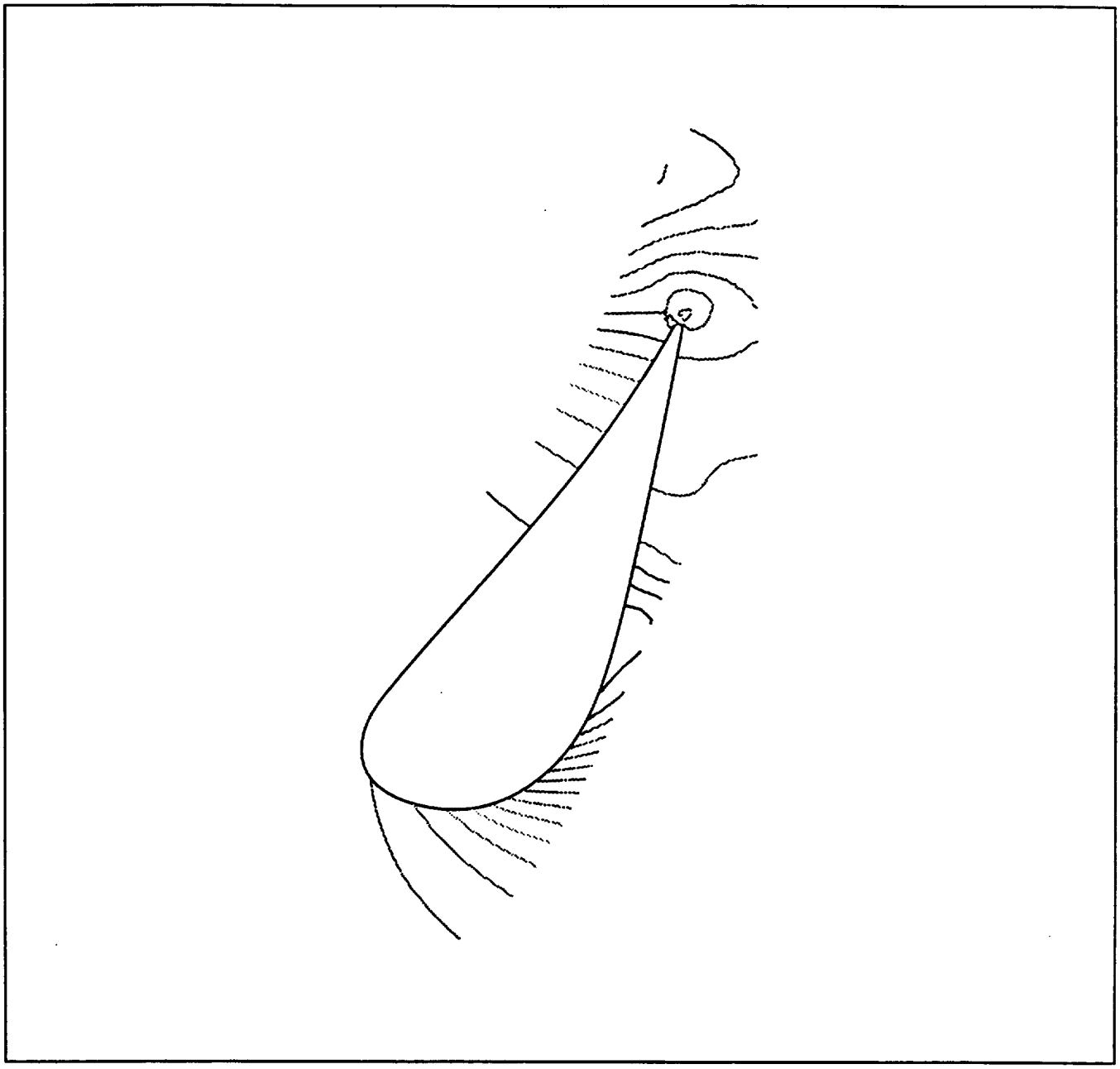

Figure 55: Instantaneous static pressure contours at midspan of HPT vane - EMD

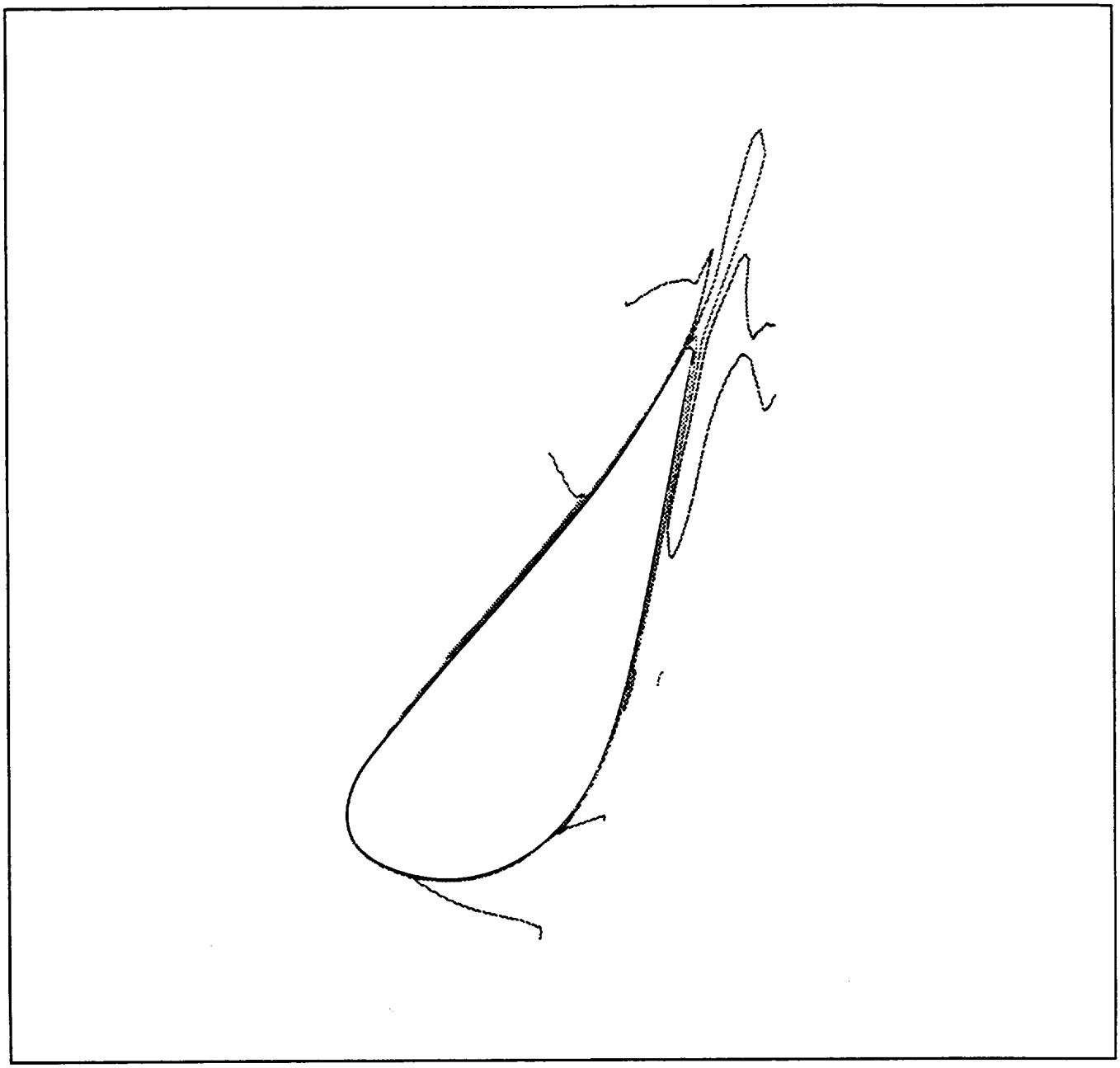

Figure 56: Instantaneous entropy contours at midspan of HPT vane - EMD

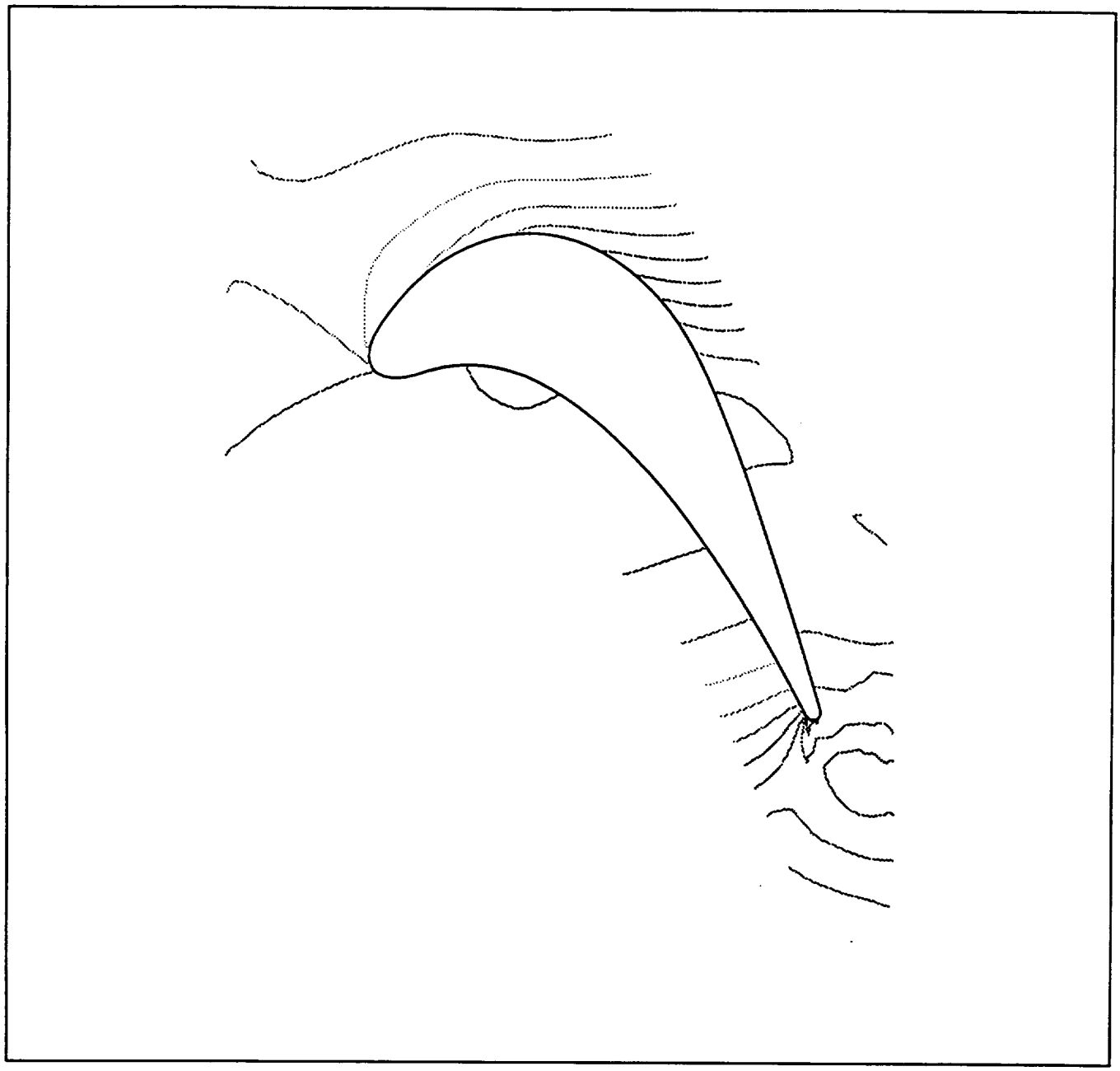

Figure 57: Instantaneous static pressure contours at midspan of HPT blade - EMD

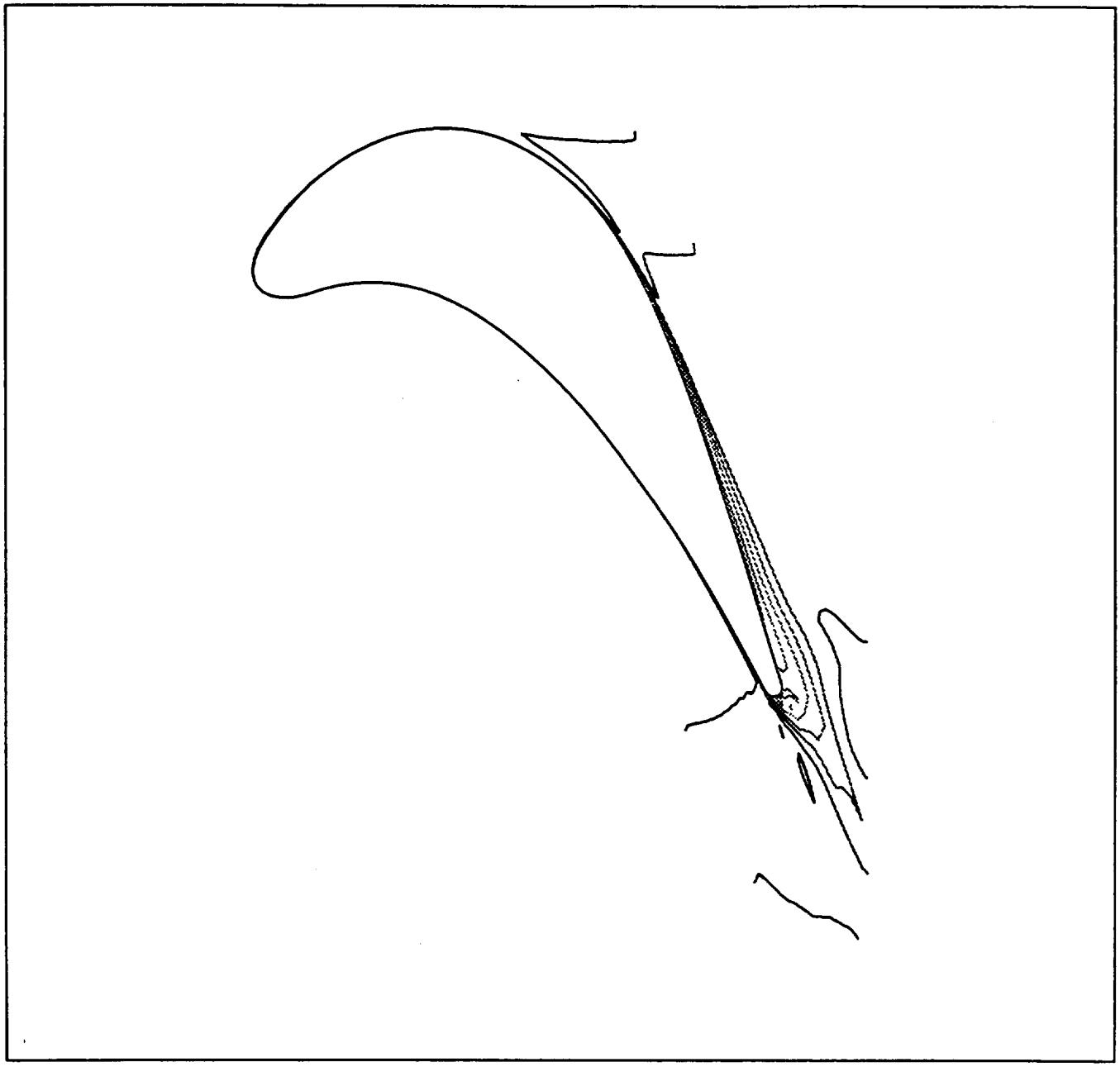

Figure 58: Instantaneous entropy contours at midspan of HPT blade - EMD

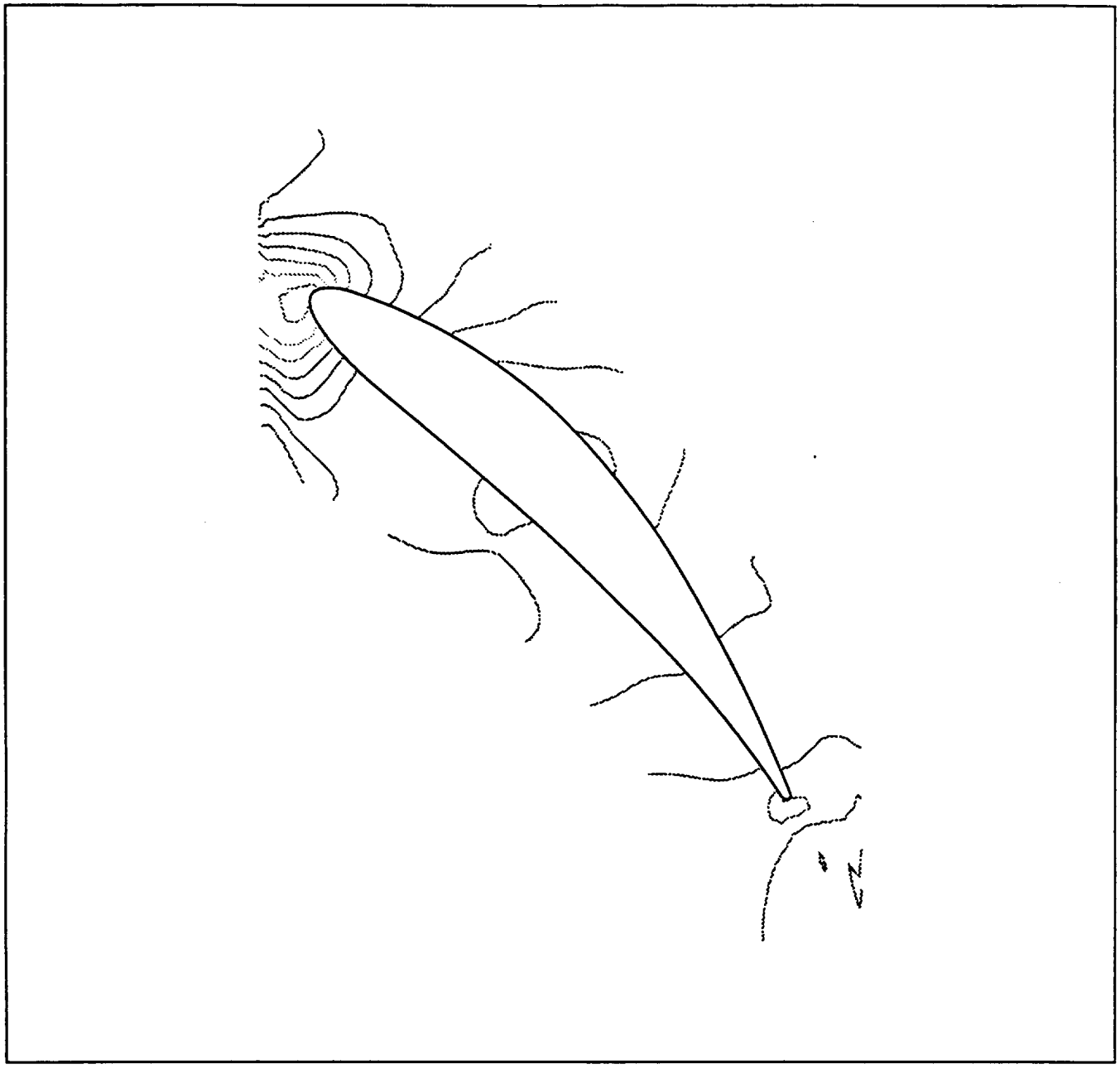

Figure 59: Instantaneous static pressure contours at midspan of LPT vane - EMD

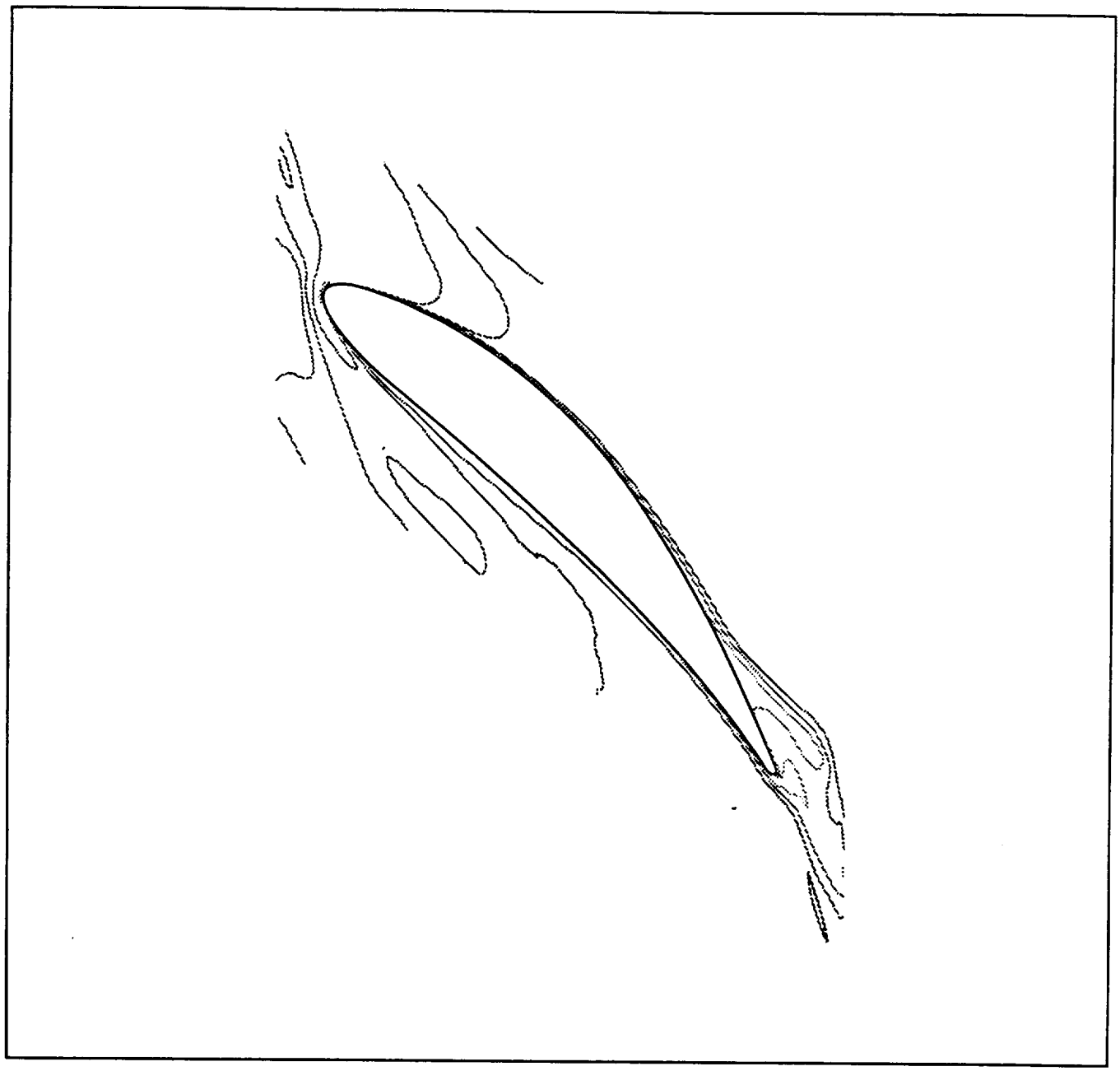

Figure 60: Instantaneous entropy contours at midspan of LPT vane - EMD

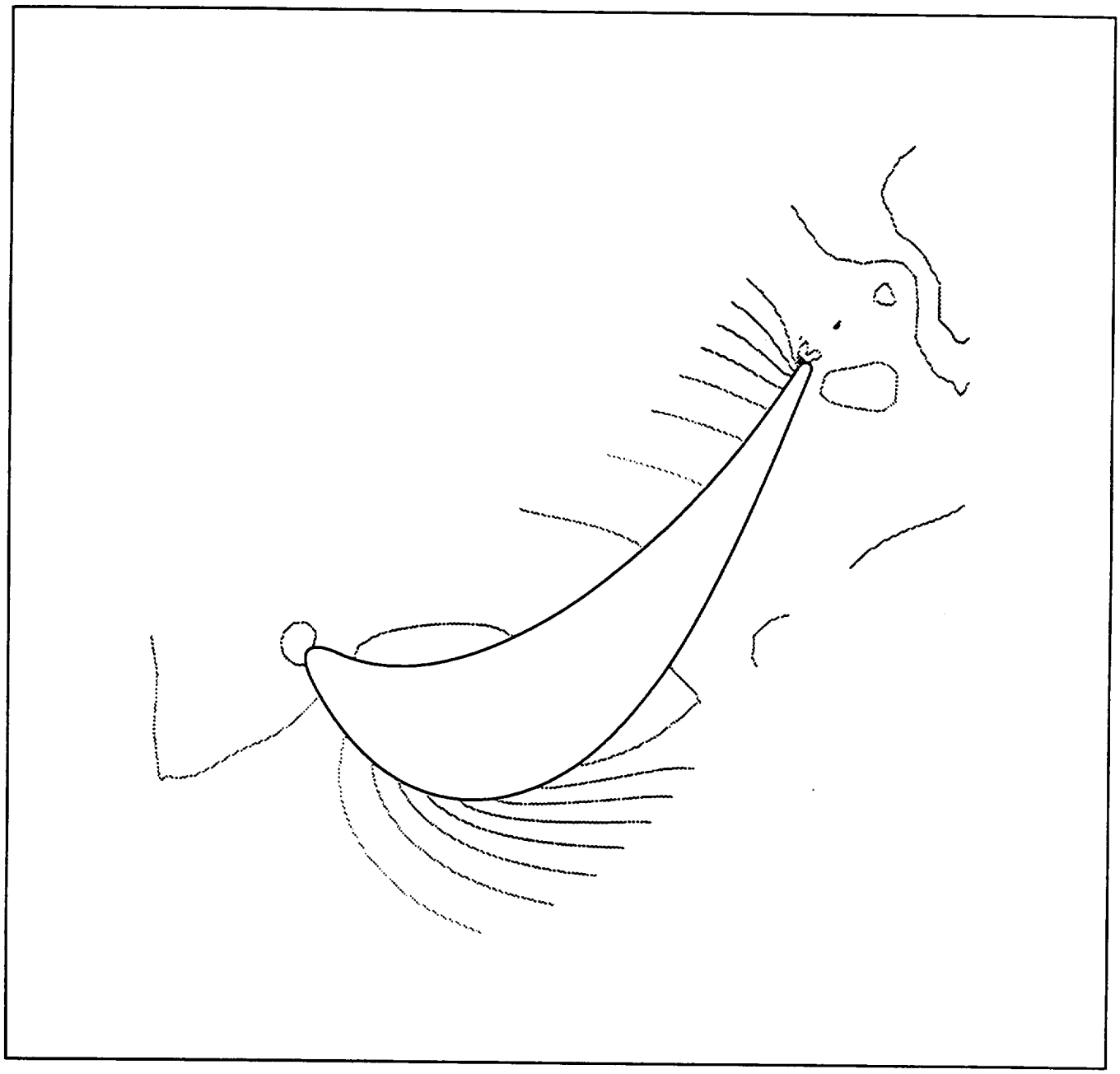

Figure 61: Instantaneous static pressure contours at midspan of LPT blade - EMD

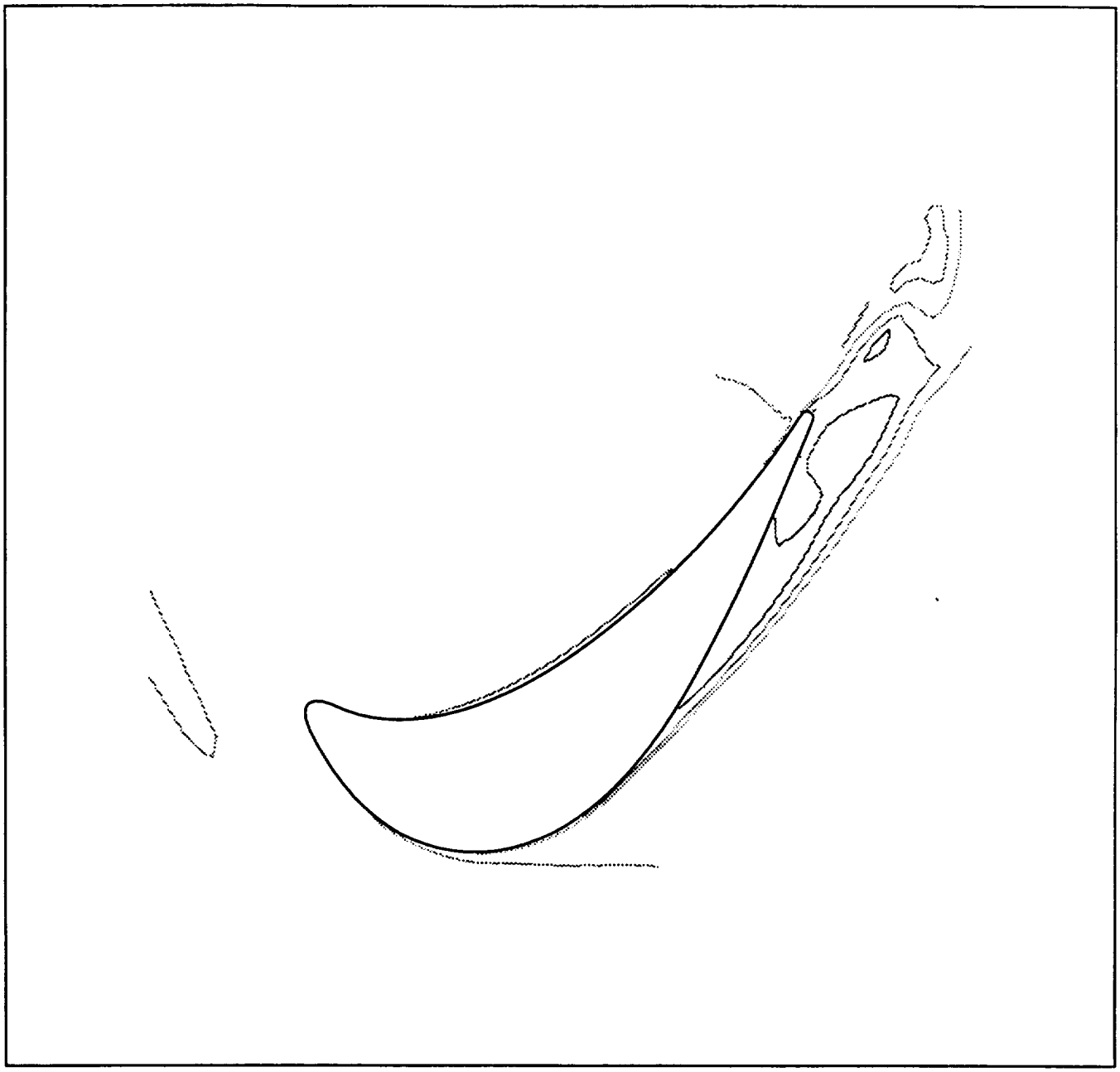

Figure 62: Instantaneous entropy contours at midspan of LPT blade - EMD

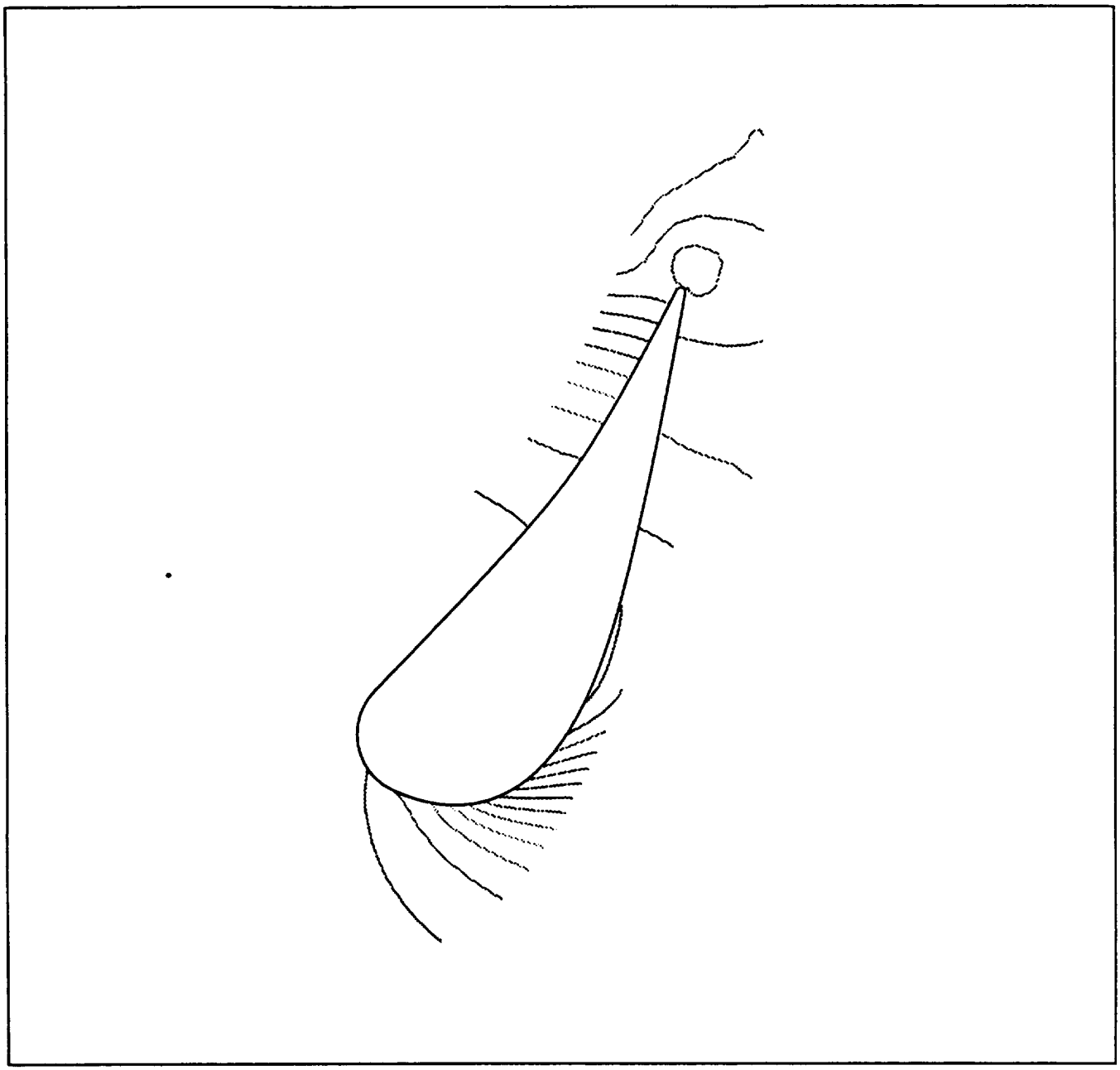

Figure 63: Instantaneous static pressure contours at midspan of HPT vane - FFR

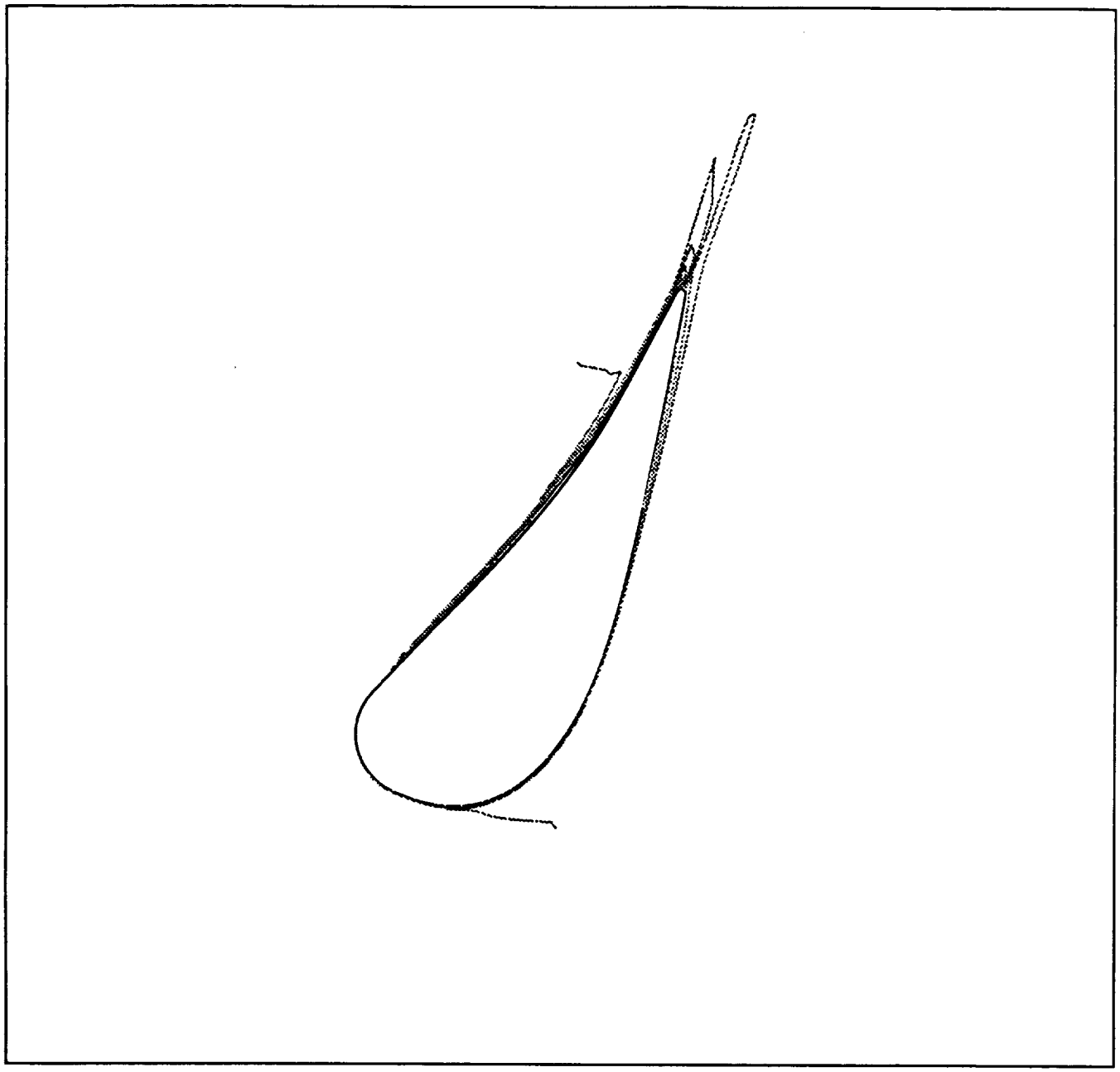

Figure 64: Instantaneous entropy contours at midspan of HPT vane - FFR

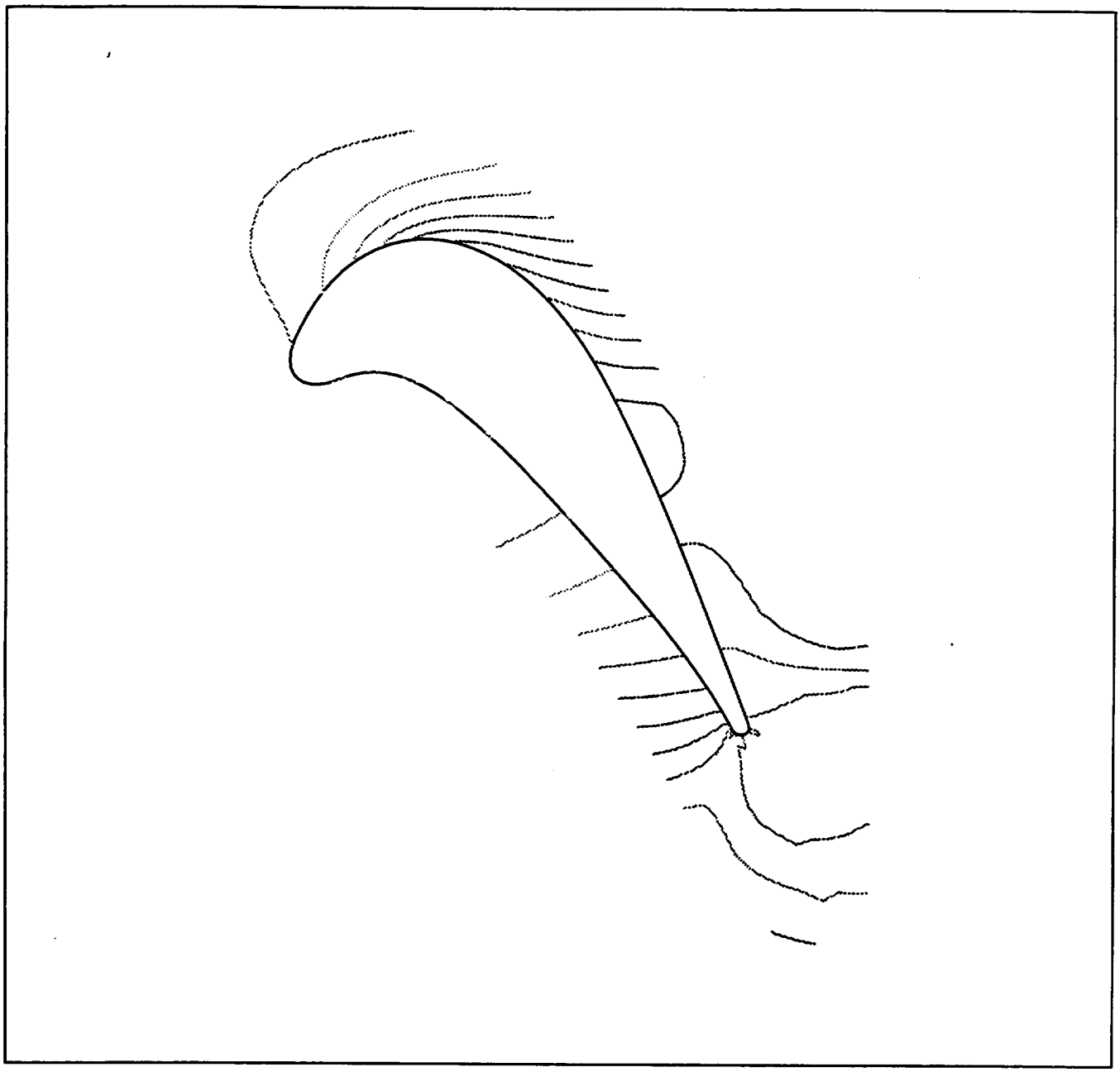

Figure 65: Instantaneous static pressure contours at midspan of HPT blade - FFR

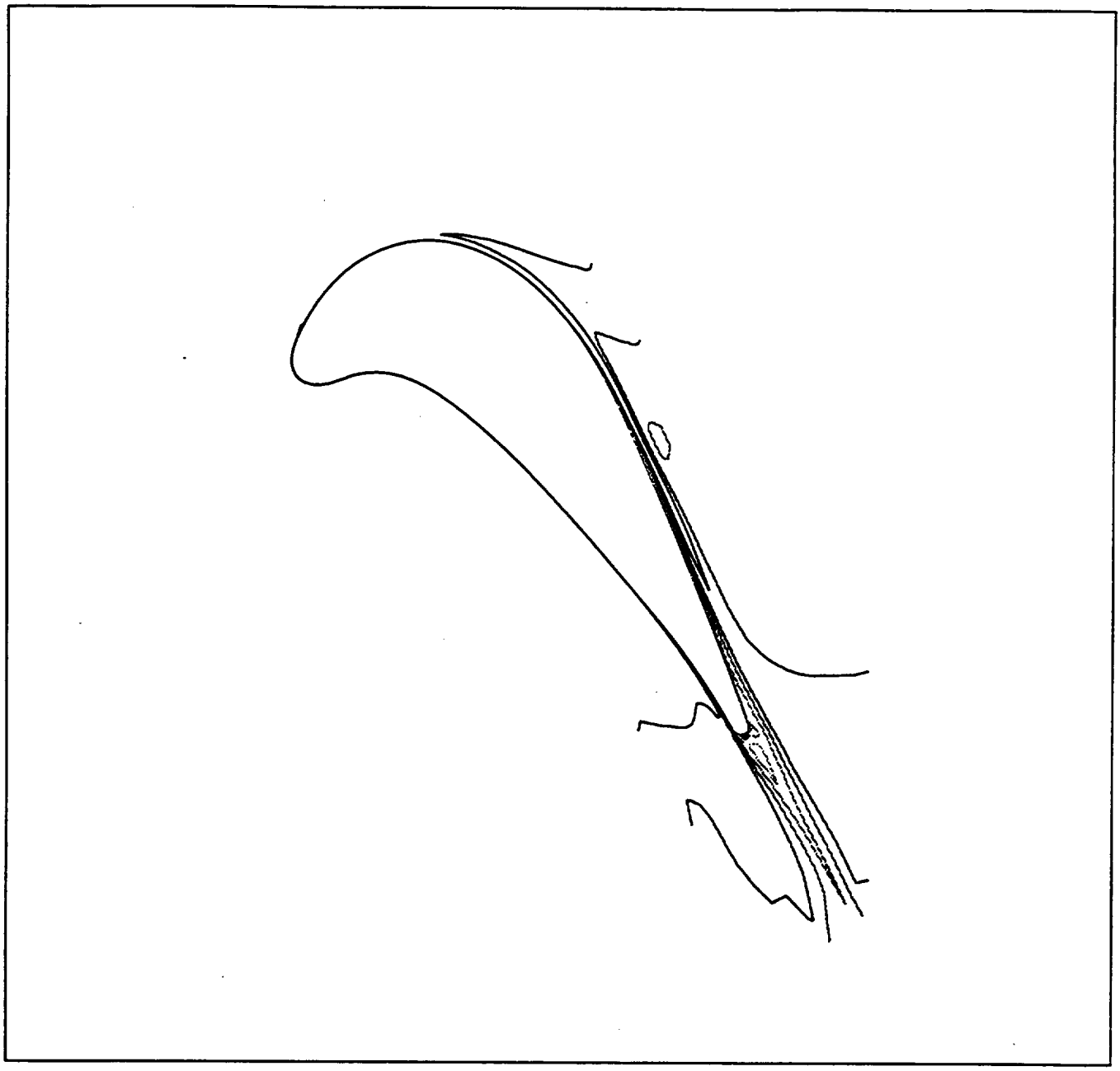

Figure 66: Instantaneous entropy contours at midspan of HPT blade - FFR

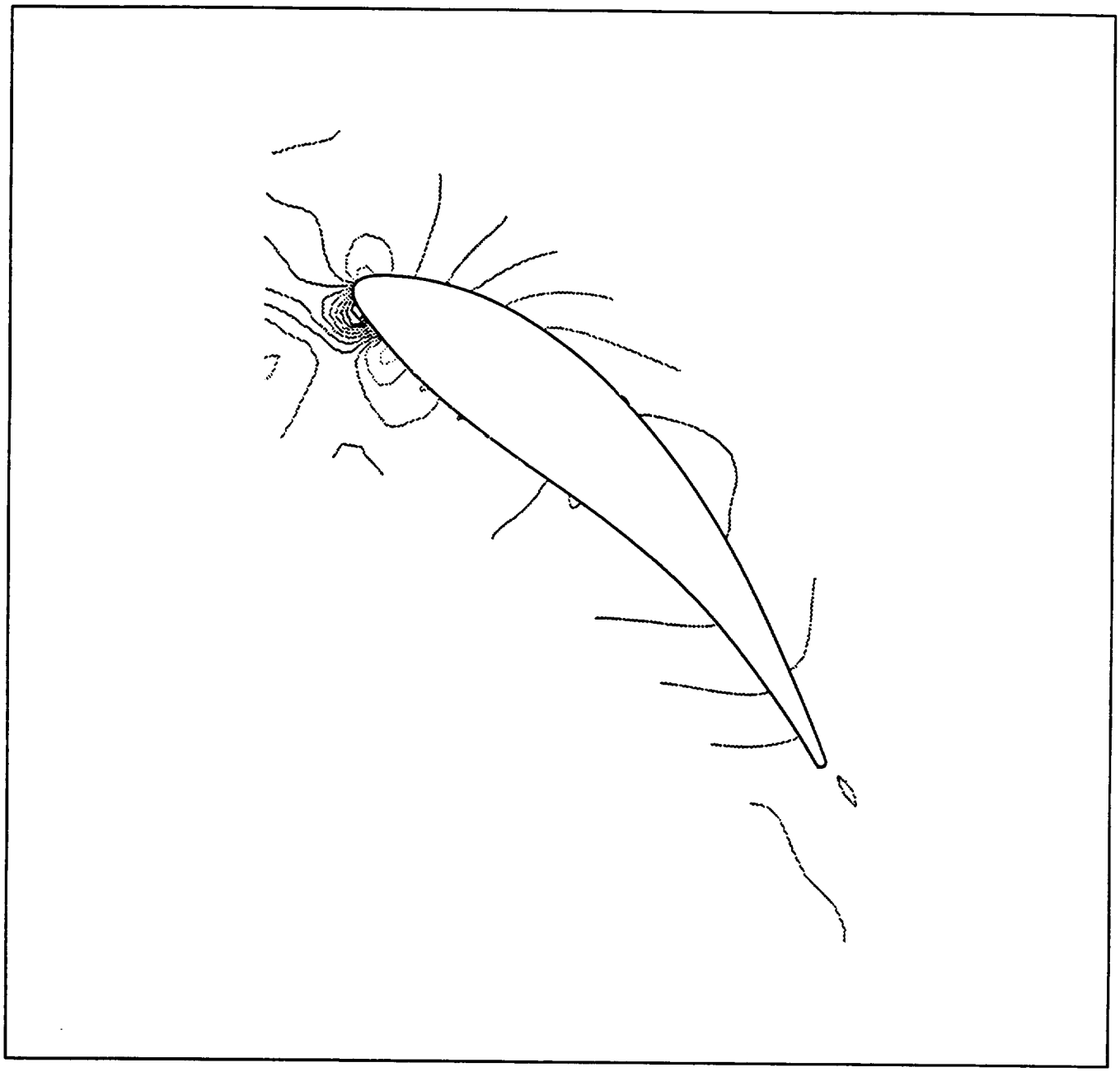

Figure 67: Instantaneous static pressure contours at midspan of LPT vane - FFR

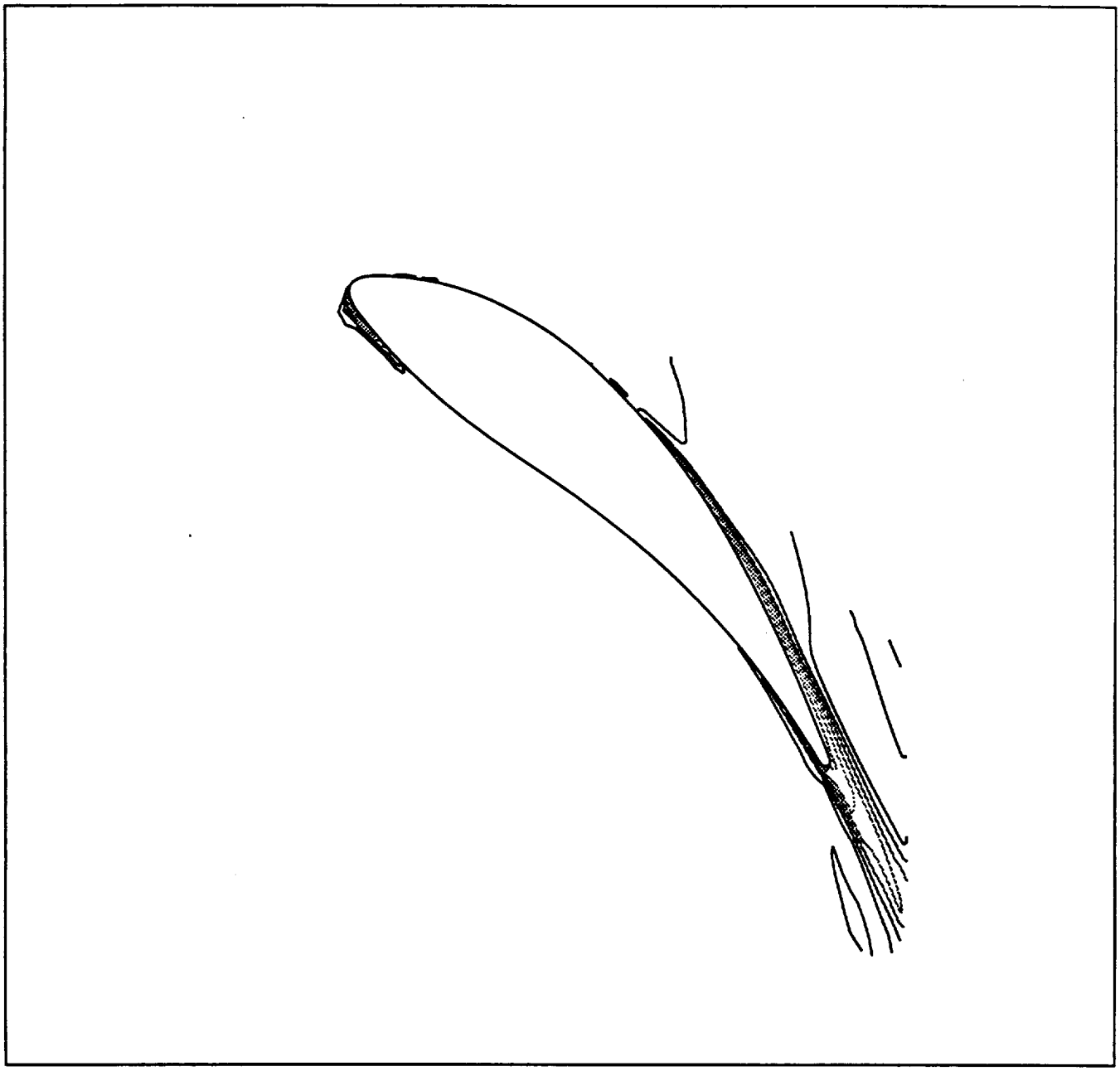

Figure 68: Instantaneous entropy contours at midspan of LPT vane - FFR

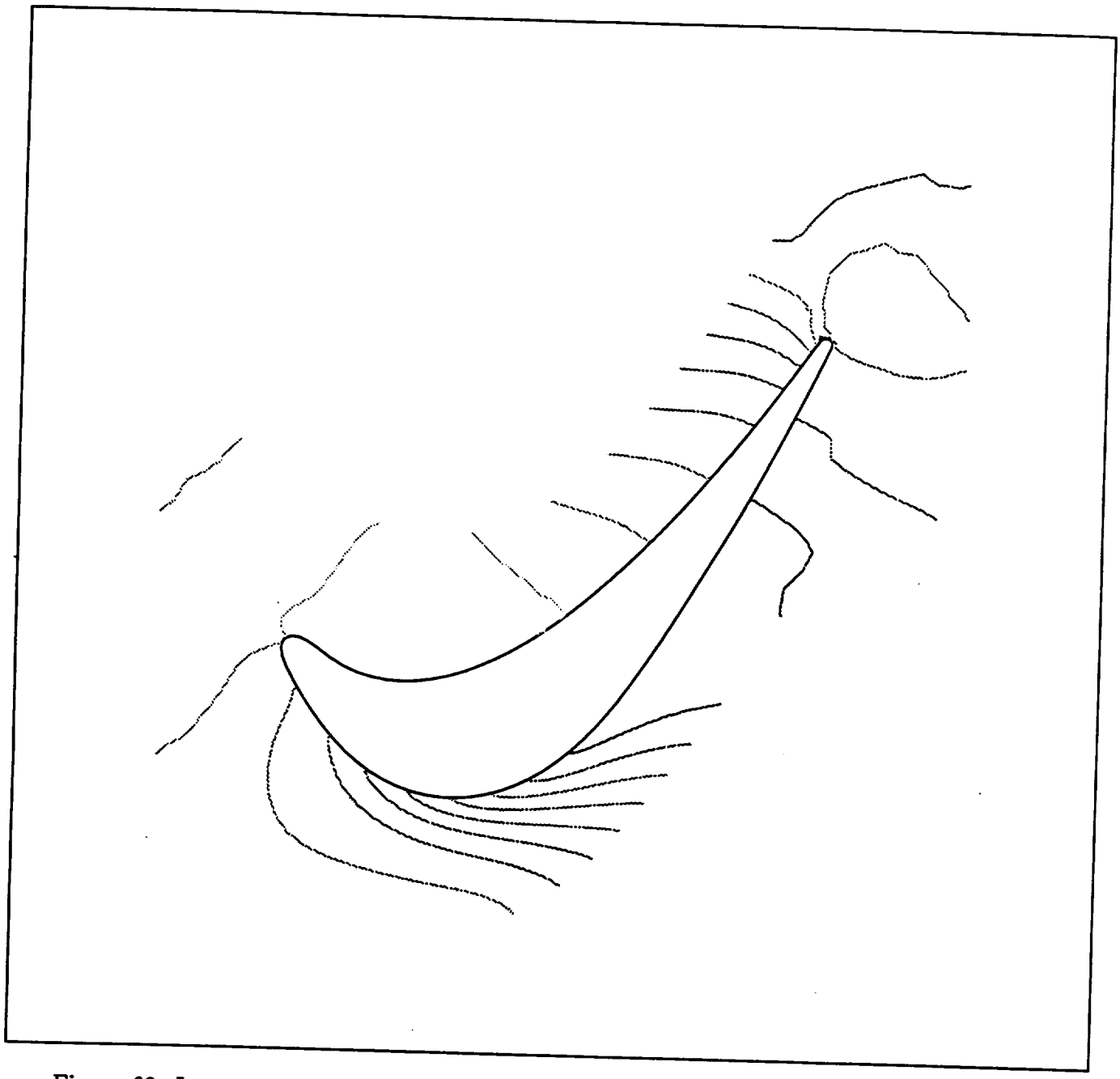

Figure 69: Instantaneous static pressure contours at midspan of LPT blade - FFR

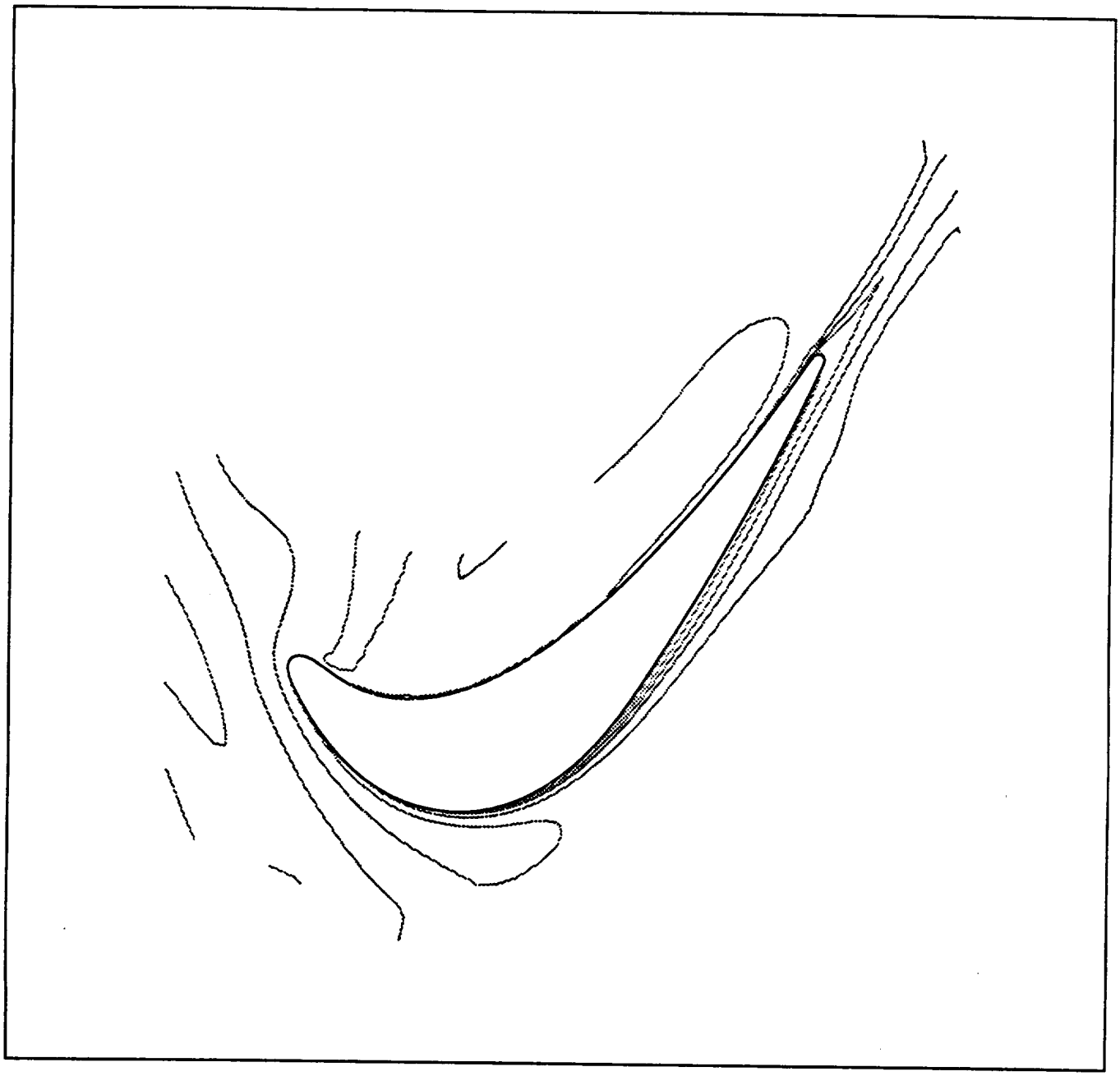

Figure 70: Instantaneous entropy contours at midspan of LPT blade - FFR